**Master's Thesis of Agriculture**

# Synthesis of gold nanoparticle-decorated single-walled carbon nanotube as a surface-enhanced Raman scattering probe for detecting wound signaling molecules in plants

식물 내 상처신호분자 검출을 위한 금 나노입자-단일벽 탄소나노튜브 기반 표면증강라만산란 센서 합성

**February 2023**

**College of Agriculture and Life Sciences**
**Seoul National University**
**Department of Agriculture, Forestry and Bioresources**

**Young Woo Han**

# Synthesis of gold nanoparticle-decorated single-walled carbon nanotube as a surface-enhanced Raman scattering probe for detecting wound signaling molecules in plants

**Advised by Prof. Kwak, Seon yeong**

**Submitting a master's thesis of Agriculture**

**November 2022**

**College of Agriculture and Life Sciences**
**Seoul National University**
**Department of Agriculture, Forestry and Bioresources**

**Young Woo Han**

**Confirming the master's thesis written by Young Woo Han**

**February 2023**

Chair _____Hyun, Jinho_____(Seal)

Vice Chair _____Kwak, Seonyeong_____(Seal)

Examiner _____Shin, Sung chul_____(Seal)

# Abstract

Detection of the plant signaling molecules before developing visible symptoms is important for early diagnosis of the plant's disease. In this study, a single-walled carbon nanotube (SWNT)-based surface-enhanced Raman scattering (SERS) nanosensor was fabricated for detecting plant signaling molecules under abiotic stress. SWNT was functionalized with a single-strand DNA (ssDNA) to prepare a SERS template, which provided binding sites for positively charged gold nanoparticles (AuNPs). Initially, AuNPs were grown on the surface of SWNT, but this process was relatively uncontrollable and caused large agglomerates. On the other hand, positively charged poly (diallyldimethylammonium chloride) capped AuNPs (PDDA-AuNPs) could densely assemble along the sidewall of the SWNT through electrostatic interaction and create a large number of hot spots. *In vitro* SERS spectra of the endogenous plant signaling molecules such as nasturlexin B, thiamine, and ATP were obtained using the nanosensor, and distinct SERS bands of each analyte were shown in the SERS spectra. Biocompatibility of the nanosensor in living plants was demonstrated by measuring the chlorophyll contents and propidium iodide (PI) assay. The strong G band of the SWNT identified the location of the nanosensor in the plants. In addition, the SERS band of the nasturlexin B, one of the plant stress signaling molecules, was presented in SERS mapping obtained upon wounding the leaf. Through our study, plant stress was detected in advance using a SERS nanosensor, which will be of

great help in preventing crop loss by monitoring continual plant stress.

**Keywords :** Surface-enhanced Raman scattering, Nanosensor, Stress-dependent signaling molecules, Biocompatibility, Single-walled carbon nanotube, gold nanoparticles

**Student Number :** 2021-21400

# Table of Contents

# List of Figures

# I. INTRODUCTION

As the Earth's population grows, the global crop demand is increasing rapidly [1]. According to a report from the Food and Agriculture Organization of the United Nations (FAO), close to 10% of the world's 8 billion people are malnourished due to the lack of food, and land and water resources related to agriculture are reaching their limit [2]. In addition, it is also predicted that there will be an additional 2 billion people by 2050 [2]. Therefore, increasing the food supply is essential to address the hunger problem and meet future demand for food. However, several biotic and abiotic stresses hinder crops' growth and interrupt stable crop production [3].

Stress in crops is the cause of plant disease and arouses diverse metabolic dysfunction [4]. Biotic stress is caused by living biological organisms such as fungi, bacteria, viruses, and insects [4-6]. When insects or herbivores attack plants, pathogens easily invade the plants through the wounded area. On the other hand, abiotic stress is triggered by environmental factors like climate change or the inflow of chemicals from outside [3, 4]. Recently, severe natural disasters have frequently occurred around the world. For example, European countries such as Germany and France have suffered from drought caused by the increased temperature, and Korea was damaged by torrential rain. These

natural disasters have a devastating impact on the food supply. In addition, the abuse of pesticides generates environmental and economic costs [7] and adversely affects the metabolic pathways of plants, such as photosynthesis, respiration, and enzyme activity [8, 9]. Therefore, overusing pesticides severely interferes with crops' growth and the food supply's enlargement. In order to prevent crop loss by these stresses, detecting the stress-induced molecules in plants is important.

Plants do not visibly express their health status, unlike humans and animals, which indicate it by voice or facial expression. Instead, plants have their defense signaling pathway to counter plant diseases and stresses [10, 11]. They activate the defense-signaling system under stress and release some stress-dependent signaling molecules before visible symptoms [12]. Therefore, detecting plant defense signals is crucial for monitoring plant health. Researching innovative methods to detect plant stress signals will be a great help for a drastic increase in the crop supply.

Various stress-dependent signaling molecules work for plants to activate defense signaling pathways [13]. The type of released biological molecules varies depending on different conditions [14]. For example, extracellular adenosine triphosphate (eATP) plays an important role in plants' defense pathways when viruses or pathogens invade plants and affects the salicylic acid level, which activates the plant defense system [15, 16]. In addition, the concentration of eATP changed when insects or herbivores physically

attacked plants because viruses and pathogens quickly infect through scratch. Thiamine, known as vitamin $B_1$, plays an essential role in the plant defense system [17], which is released in response to different abiotic stresses like cold, osmotic, and salinity conditions [18]; also, it has been used as a control agent for different diseases, including charcoal rot disease and sheath blight disease [18]. Nasturlexin B is cruciferous aromatic phytoalexins released by watercress against abiotic stress [19, 20], which is produced to activate the antifungal signaling systems of crucifers [19]. The concentration of reactive oxygen species (ROS) rapidly increases under stress due to biotic and abiotic stimuli since ROS makes plants defend against different stresses [21]. For example, $O_2^{\cdot -}$ and $^1O_2$ are produced by the photosystems I and II in chloroplasts when the plant is under excess light stress or drought stress, and the plants immediately activate their defense system [22].

Nanosensor is suitable for *in vivo* monitoring of endogenous biological molecules because it is nondestructive, and the intrinsic optical and electrical properties can be used as outputs for the signal [23]. Previous studies fabricated various nanosensors to detect plant signaling molecules [24-27]. They used different strategies, such as measuring changes in fluorescence or temperature. However, these nanosensors detected only a few signaling molecules, so another approach is needed to monitor a variety of plant signaling molecules. Surface-enhanced Raman scattering (SERS) can be a powerful analytical tool for recognizing various induced signaling molecules.

However, detecting the specific signaling molecules upon stress has been challenging because of their low concentration and coexistence with other biological molecules. SERS-based nanosensors can detect a trace amount of analytes by collecting multiple biological molecules simultaneously because of their high sensitivity and fingerprint spectral pattern. If the SERS signal can be obtained from an optically active SERS probe in the near-infrared near-infrared (NIR) region, it can avoid strong background fluorescence due to chlorophyll from deeper plant tissues [28].

In this study, a nondestructive carbon nanotube-based SERS nanosensor was designed for detecting and identifying endogenous plant signaling molecules in living plants. *In vivo* SERS nanosensor consisted of a single-walled carbon nanotube (SWNT) and gold nanoparticles (AuNPs) as SERS template and substrate, respectively, to enhance Raman intensity of the plant signaling molecules. It was also expected to be biocompatible in the living plants and active in the NIR region to avoid background noise from chlorophyll in deeper tissue. Finally, I aimed to monitor the plant signaling molecules in living plants after wound stress using this SERS nanosensor.

# II. LITERATURE SURVEY

## 2.1. Surface-enhanced Raman scattering (SERS)

### 2.1.1. Principle of SERS

The SERS phenomenon amplifies Raman scattered light of molecules by metal nanoparticles (MNP) [29]. When a specific laser frequency is irradiated to the metal, electron clouds on the surface oscillate; this phenomenon is surface plasmon resonance (SPR) [30]. SPR usually occurs in a localized part of MNPs like Ag, Au and Cu nanoparticles, called localized surface plasmon resonance (LSPR).

LSPR generates a strong electromagnetic field on the surface of the MNP and the Raman scattered light enhancement is caused by electromagnetic fields [31]. A more powerful electromagnetic field is generated in the gap between the MNPs due to coupled electron clouds of each MNP [32]. Raman intensity from the interparticle junction is more enhanced by 2 to 4 orders than enhanced Raman intensity by a single nanoparticle [33, 34]. The magnitude of Raman signal enhancement depends on the particles' size, shape, and electron density [31]. In addition, a stable and uniform arrangement of MNP is needed for the reproducibility and steadiness of the SERS signal [35].

### 2.1.2. Biological application of the SERS

SERS has been used to detect trace amounts of analytes because of its high sensitivity. Furthermore, Raman spectroscopy can analyze multiple analytes simultaneously because each has a nonoverlapping fingerprint spectral pattern with narrow bandwidth [36]. Therefore, numerous researchers have used SERS technology for biosensors [37, 38], therapeutic drug monitoring [39, 40], monitoring intercellular environments [41, 42], and cell imaging [43, 44] in the biological field. Here I listed several examples of the biosensor application using SERS.

Li *et al.* reported a 3D SERS substrate for mycotoxin detection inspired by cauliflower morphology [45]. Mycotoxin is a metabolite produced by micro-sized fungi that contaminate food resources, especially maize [45, 46]. This nanosensor detected three kinds of mycotoxin at once due to sputtered AuNPs. Each fingerprint SERS band of the mycotoxins was presented in the SERS spectrum. Yang *et al.* fabricated 4-Mercaptophenylboronic acid (4-MPBA) functionalized AuNPs and deposited them on a ZnO nanowire to detect glucose [47]. Glucose formed a complex with the 4-MPBA by interaction with the hydroxyl group in the 4-MPBA through a dehydration reaction. As a result, the SERS band of the 4-MPBA at 1071 and 1098 $cm^{-1}$ shifted to the SERS band at 1084 $cm^{-1}$. They accurately detected the glucose in the aqueous humor of ex vivo rabbit eyes up to 1 mM. Andreou *et al.* rapidly detected drugs in saliva by SERS and microfluidics [48]. Salt was

used to cause aggregation of silver nanoparticles (AgNPs) for creating hot spots. Methamphetamine was rapidly detected by amplified Raman peak at 1261 and 1409 $cm^{-1}$.

## 2.2. Carbon nanomaterial for SERS template

Carbon is an interesting element that can be present in different allotropes [49]. Carbon nanotube (CNT), graphene, carbon dot, and fullerene are in the spotlight from various studies and industries because they have unique optical and electrochemical properties [49-51]. Carbon nanomaterials also act as fluorescence quenchers to achieve high signal-to-noise ratios in biological samples, making them appropriate for biosensors [52, 53]. Among them, single-walled carbon nanotubes (SWNT) and graphene oxide (GO) were used as SERS templates where many MNPs were densely assembled in previous studies due to their high surface area [43, 44, 54-58].

### 2.2.1. Utilization of SWNT as a SERS template

SWNT is a carbon nanotube that consists of one layer of graphene with diameters of 0.4~2nm and lengths of several centimeters [59]. SWNT has a high surface area, aspect ratio and intrinsic near-infrared (NIR) fluorescence [60]. A strong G band at 1500~1600 $cm^{-1}$ in the Raman spectrum of SWNT has been used to examine biological samples such as cancer cells and hazardous bacteria [43, 57, 61, 62]. Therefore, it has been used for biological and medical applications [63, 64], optical sensors [25, 65, 66], and delivery

carriers [67-69]. Since SWNT tends to aggregate in aqueous solution due to high van der Waals force and π-π interaction between SWNT [70], functionalization of SWNT is necessary for biological application. SWNT can be functionalized covalently or noncovalently to increase dispersity and stability in an aqueous solution [70-72].

SWNT is covalently functionalized with various polymers and organic molecules by oxidation [73]. Liu *et al.* functionalized SWNT with hydrophilic poly(ethylene glycol) (PEG) [74]. SWNT is functionalized by covalent bonding between carboxylic groups of PEG and the sidewall of oxidized SWNT. Palacin *et al.* bind zinc porphyrins to oxidized SWNT by click chemistry of azide and alkyne [75]. Click chemistry is an effective tool for SWNT covalent functionalization thanks to high yields and mild reaction conditions [76]. However, the defect of SWNT by oxidation which is necessary for the covalent functionalization of SWNT, affects the structural stability and electronic properties of SWNT [77]. Setaro *et al.* proposed new covalent functionalization of SWNT to preserve electronic properties at a level similar to that of pristine SWNT [78]. When they used a [2+1] reaction between the azidodichloro-triazine and the sidewall of the SWNT, the resultant covalently functionalized SWNT maintained the $sp^2$ characteristic of SWNT.

Noncovalent modification of SWNT with aromatic compounds or polymers by π-π interaction or hydrophobic interaction could preserve the

properties of SWNT [72]. Zheng *et al.* produced single-strand DNA (ssDNA) wrapped SWNT [79]. Aromatic nucleotide bases in ssDNA strongly bind to SWNT by π-π stacking interactions. Furthermore, a negative charge on the surface of SWNT by phosphate groups in ssDNA results in electrostatic repulsion, which helps the dispersion of SWNT. Simmons *et al.* noncovalently attached pyrenecarboxylic acid (PCA) to the SWNT surface by π-π stacking interactions between the pyrene moiety of PCA and the SWNT sidewall [80]. PCA-SWNT is stably dispersed in water due to polar carboxylic acid groups of PCA, so it can substitute oxidative acid treatment of SWNT, damaging the structure of SWNT.

A dense and uniform assembly of MNPs on the SERS template is essential to enhance the Raman intensity of analytes. SWNT is commonly used as a SERS template due to its high surface area and easy functionalization [54]. Furthermore, SWNT is biocompatible; thus, it is appropriate for detecting biological molecules *in vivo* [50]. Ondera *et al.* decorated SWNT with popcorn-shaped gold nanoparticles (AuNPs) [57]. They covalently bonded 4-aminothiophenol, which has thiol groups that highly interact with AuNPs, to the side wall of SWNT. AuNPs were uniformly and tightly attached to the SWNT through a strong bond between AuNPs and thiol groups of the 4-aminothiophenol. Raman intensity of the SWNT G band was enhanced due to assembled AuNPs. Song *et al.* used a carbon nanotube ring (CNTR) as a SERS template [44]. They coiled SWNT to ring structure

for higher surface area and dispersity in an aqueous solution. Thus, CNTR-AuNP composites showed a stronger Raman signal than straight SWNT-AuNP composites because more AuNPs are attached to CNTR than straight SWNT. Wang *et al.* reported gold nanoparticles (AuNPs) and single-walled carbon nanotube (SWNT) nanocomposites for cancer cell imaging and photothermal therapy [43]. Enhanced SWNT Raman G-band shortens the Raman imaging time of cancer cells.

### 2.2.2. Utilization of graphene as a SERS template

Graphene has a structure where carbon atoms are gathered to form a two-dimensional plane [81]. Each carbon atom forms a hexagonal lattice with carbon atoms positioned at the vertices of the hexagon. It has a large surface area, high conductivity, and elastic modulus [82]. Graphene oxide (GO) is obtained through the oxidation of graphite by chemical treatment [83]. GO can provide many binding sites for MNPs because oxygen groups on the graphene enable additional chemical modification [84]. In addition, graphene enhances the Raman signal by chemical enhancement mechanism, so graphene-MNP can powerfully enhance Raman intensity [50, 84, 85].

Iliut *et al.* synthesized GO-AuNPs composite by ascorbic acid, which can reduce both Go and Au ions [86]. Oxygen groups and defect areas on the reduced GO (rGO) surface provided sites for AuNPs nucleation. Uniformly sized AuNPs were distributed on the surface of rGO, and GO-AuNPs

composite had a much higher enhancement factor than single gold nanoparticles. Hu *et al.* loaded gold nanorod (AuNR) to GO by electrostatic interaction [87]. Positively charged AuNRs (11 mV) were assembled on the negatively charged GO (-45.3 mV). UV-visible absorbance peak of GO-AuNR nanocomposite shifted to a red wavelength area and became broader due to tightly assembled AuNRs. Hsu *et al.* used microwave and L-arginine for depositing silver nanoparticles (AgNP) on the rGO [88]. Microwave irradiation increased the temperature of reagents, so it helped the formation of AgNP. AgNPs were loaded uniformly on the rGO and formed many hot spots. Therefore, AgNP-rGO detected a tiny amount of 4-aminothiophenol, and the enhancement factor was about $1.27 \times 10^{10}$.

## 2.3. Nanosensor for detecting plant endogenous signaling molecules in living plants

Several studies reported various nanosensors for detecting biological molecules from the defense systems of plants [12, 23-25, 89, 90]. They used various analytical tools like fluorescence, SERS, and temperature change to detect plant signaling molecules. Lew *et al.* detected an $H_2O_2$ signal in plants by single strand DNA-SWNT composites-based nanosensors ($(GT)_{15}$-SWNT) [25]. Intrinsic NIR fluorescence of the $(GT)_{15}$-SWNT, which can avoid autofluorescence from deeper tissue, was quenched in the presence of $H_2O_2$. After wounding, it can detect about 50 μM of $H_2O_2$ in various plant species,

including *A. thaliana*, lettuce, and arugula. Yan *et al.* fabricated a metal-organic framework (MOF)-based biosensor for detecting $H_2O_2$ signal in plants by temperature signal [24]. Horseradish peroxidase (HPR) and 2,2′-azino-bis (3-ethyl-benzothiazoline-6-sulfonic acid) (ABTS) were encapsulated by zeolite imidazolate frameworks-8 (ZIF-8). The temperature increased when HRP and $H_2O_2$ inside the plants oxidized ABTS. They detected $H_2O_2$ after abiotic stress, such as pathogen infection, heat damage, and mechanical wounding. Zhang *et al.* indirectly detected abscisic acid (ABA), one of the plant hormones, using a SERS aptamer sensor in plant fluid [91]. They attached 4-mercaptobenzoic acid (4-MBA) and ABA aptamer on the signal probe and cDNA of ABA aptamer on the capture probe. Signal probes were first anchored on the capture probe, and then signal probes were released from the probe when ABA existed; thereby, the SERS intensity of 4-MBA decreased. They monitored ABA, which was extracted from wheat leaves, through this way up to 0.67 fM.

# III. MATERIALS AND METHOD

## 3.1. Materials

$(GT)_{15}$ was purchased from Integrated DNA Technologies (Iowa, USA). Single-walled carbon nanotube (SWNT), sodium chloride (NaCl), gold (III) chloride trihydrate ($HAuCl_4$), L-ascorbic acid, Pur-A-Lyzer midi dialysis kit (MWCO 1kDa), poly (diallyldimethylammonium chloride) (PDDA, medium molecular weight, 20 wt. % in $H_2O$), sodium hydroxide (NaOH), 4-bromothiophenol (4-BBT), standard 20 nm gold nanoparticles, 4-fluorothiphenol (4-FBT), adenosine 5'-triphosphate (ATP) disodium salt hydrate, thiamine, 2-thiazoline-2-thiol (2-TAT), 2-(N-morpholino)ethanesulfonic acid (MES), magnesium sulfate ($MgSO_4$), perfluorodecalin, and propidium iodide (PI) were purchased from Sigma-Aldrich (St. Louis, USA).

## 3.2. Synthesis of $(GT)_{15}$-SWNT

SWNT dispersed in ethanol is washed twice with deionized water using 50 kDa ultracentrifugal filter devices at 4000 rpm for 6 min. 1 mg of $(GT)_{15}$ and 0.5 mg of SWNT were mixed in 1 ml of 50 mM NaCl. The mixture was sonicated with a 3 mm probe tip for 20 min at 40 % amplitude in an ice bath

using an ultrasonicator (VCX 130, Sonics & Materials Inc., USA) [25] and then was centrifuged twice at 16,000g for 90 min to remove the bundle of SWNT. The resulting $(GT)_{15}$-wrapped SWNT ($(GT)_{15}$-SWNT) was filtrated 5 times through 100 kDa ultracentrifugal filter devices at 4000 rpm for 6 min to remove excess DNA [43].

The charge and size of $(GT)_{15}$-SWNT were investigated with a zeta potential analyzer (Nano Zs90, Malvern Panalytical, UK) and nanoparticle tracking analysis (NTA) (Nanosight LM10, Malvern Panalytical, UK). The photoluminecescence of $(GT)_{15}$-SWNT was measured by a fluorescence spectrometer (Nanolog, HORIBA scientific, Japan). The emission of $(GT)_{15}$-SWNT was measured under excitation at 730 nm laser with 30 sec exposure time, and its absorbance was measured from 400 to 1300 nm using a UV-Vis spectrometer (UV-2600 I, Shimadzu Co., Japan). The concentration of $(GT)_{15}$-SWNT was estimated by Eq. 1.

$$(GT)_{15}\text{-SWNT concentration (mg L}^{-1}) = \frac{\text{Absorbance at 632 nm}}{0.036} \times \text{Dilution factor (Eq. 1)}$$

The concentration of free DNA $(GT)_{15}$ was estimated by a calibration curve based on absorbance at 260 nm ranging from 1 to 50 mg/L. A portion of 0.16 mg SWNT was mixed with 1 mg of (GT)15 in 1 mL of 50 mM NaCl (aq). The mixture was sonicated with a 3 mm probe tip for 20 min at 40 % amplitude in an ice bath using an ultrasonicator. From the absorbance of

filtrate $(GT)_{15}$ after filtration of $(GT)_{15}$-SWNT at 4000 rpm for 6 min five times using a centrifugal filter, the amount of $(GT)_{15}$ molecules wrapped with 1 mg of SWNT was estimated by the following Eq. 2.

$$\text{Amount of wrapped } (GT)_{15} \text{ per 1 mg of SWNT} = \frac{\text{1 mg - (Amounts of removed } (GT)_{15}\text{) (mg)}}{\text{Amounts of the } (GT)_{15}\text{-SWNT (mg)}} \quad \text{(Eq. 2)}$$

## 3.3. Gold nanoparticle growth on $(GT)_{15}$-SWNT

500 μL of $(GT)_{15}$-SWNT (20 mg/L) and 250 μL of $HAuCl_4$ (240 mM) were mixed and continued to stir at 25 °C at 800 rpm for 60 min. The mixture was dialyzed with 1 kDa MWCO dialysis membrane overnight. Next, 125 μL of $HAuCl_4$ (0, 0.8, 4, 8, and 40 mM) and L-ascorbic acids (640 mM) were added and continued to react at 25 °C at 800 rpm for 30 min [92]. The mixture was dialyzed using 1 kDa MWCO dialysis membrane overnight, hereafter AuNP@SWNT. The SERS spectrum of 4-BBT was acquired by a Raman microscope system (LabRAM 200VN, Horiba, Japan) equipped with a 660 nm laser and capillary tube. The laser power was 25 mW, and the exposure time was 10 sec with an x10 objective lens. The morphology of AuNP@SWNT was investigated using transmission electron microscopy (TEM, JEM1010, JEOL, Japan). 10 μL of the AuNP@SWNT was dropped on copper carbon film 300 mesh (CF300-Cu-50, Electron microscopy sciences, USA) 10 times.

## 3.4. Fabrication of PDDA-AuNP@SWNT

200 μL of NaOH (0.5 M), 100 μL of $HAuCl_4$ (10 mg/mL), 200 μL of PDDA (20 wt%) and 20 mL of deionized water were stirred at 25 °C at 800 rpm for 5 min [93]. This solution was then stirred at 100 °C at 400 rpm for 60 min until the color changed to ruby red and then was washed 5 times with deionized water by centrifugation at 15 °C at 14500 rpm for 45 min to remove excess PDDA [94]. These gold nanoparticles were denoted as PDDA-AuNPs.

The concentration standard curve of 20 nm gold nanoparticles was acquired by UV-Vis spectrometer. The absorbance of 20 nm gold nanoparticles at 520 nm was measured between 8.7 x $10^9$ and 6.54 x $10^{11}$ particles/mL for 13 points. This standard curve was used to estimate the concentration of the PDDA-AuNPs. Zeta potential analysis was performed to confirm the charge of the PDDA-AuNPs. Micrographs of PDDA-AuNPs were obtained using TEM, and the diameter of the PDDA-AuNPs was analyzed using the ImageJ program (1.52a, National Institutes of Health, USA). 10 μL of the PDDA-AuNP was dropped on copper carbon film 300 mesh (CF300-CU, Electron Microscopy Sciences, USA) on the filter paper 10 times.

100 μL of $(GT)_{15}$-SWNT (35 mg/L), 500 μL of PDDA-AuNPs (1.0 x $10^{12}$, 2.0 x $10^{12}$, 3.0 x $10^{12}$, and 4.0 x $10^{12}$), and 400 μL of deionized water were vortexed for 5 sec until the color changed to purple. The charge and

morphology of PDDA-AuNP@SWNT were analyzed by zeta potential analyzer and TEM, respectively.

## 3.5. *In vitro* SERS spectrum acquisition

3.5 mg/L of PDDA-AuNP@SWNT was mixed with 4-FBT 1 mM at 25 °C at 800 rpm for 1 h. Raman microscope system (LabRAM 200VN, Horiba, Japan) equipped with a 660 nm laser and capillary tube. The power of the laser was 25 mW, and the exposure time was 60 sec with an x10 objective lens.

3.5 mg/L of PDDA-AuNP@SWNT was mixed with plant stress-dependent biomolecules such as 100 μM ATP, thiamine, and 2-TAT. SERS spectra were obtained by Raman microscope (XperRAM S Series, Nanobase, Korea) equipped with a 785 nm laser and a silicon wafer (4-inch Silicon Wafer, Silicon Technology Corporation, Japan). A portion of 10 μL of the chemical mixture was dropped onto the silicon wafer and dried for 1h. The power of the 785 nm laser was 13 mW, and the exposure time was 100 milliseconds with an x50 objective lens.

## 3.6. Plant growth

These experiments were carried out with 3- to 4-week-old laboratory-grown plants. I counted the plant age from seeding. Commercial watercress (*Nasturtium officinale*) was seeded in disposable pots filled with standard

culture soil. Watercress was grown in a plant growth chamber (HB-303DH-O, Hanbaek Scientific Co., Korea) with conditions set at 70% humidity, 23 °C, medium light intensity (5-10 mW cm-2), and 16 h light/8 h dark cycles.

## 3.7. Biocompatibility of PDDA-AuNP@SWNT in plants

3.5 mg/L of PDDA-AuNP@SWNT in 5 mM MES-$MgSO_4$ buffer (pH 5.7) was infiltrated into the watercress leaf. Leaf chlorophyll contents were measured using a SPAD meter (Minolta, 592 Plus, Japan) once a week. Propidium iodide assay was carried out to evaluate the biocompatibility of the nanosensor at the cellular level and analyzed using confocal fluorescence microscopy imaging (CLSM SP8 X, Leica, Germany). PDDA-AuNP@SWNT (3.5 mg/L) in MES-$MgSO_4$ buffer (5 mM, pH 5.7) or the buffer alone was infiltrated into leaves through the abaxial side. The leaf was cut 1 h after infiltration, and a leaf disc (5 mm in diameter) was prepared. The leaf disc was immersed in propidium iodide solution (10 mg/L) for 10 min and then transferred to a glass slide with a polydimethylsiloxane (PDMS, Carolina Observation Gel, NC, USA) chamber filled with perfluorodecalin on a glass slide. The slide was sealed with a coverslip and imaged with an x40 water immersion objective lens. Microscopic images of the watercress epidermis area were acquired by a fluorescence microscope (Ts2 FL, Nikon, Japan) with x10 and x40 objective lenses.

## 3.8. Monitoring of endogenous stress-dependent biomolecules

## in living plants

3.5 mg/L of PDDA-AuNP@SWNT in 5 mM MES-$MgSO_4$ buffer (pH 5.7) was infiltrated into the watercress by 1 mL syringe and dry for 1 h. After that, the leaf surface was wounded by the sharp stick. SERS mapping with a 785 nm laser was measured at least 700 μm away from the wound. SERS mapping images of the watercress leaf epidermis were obtained using a confocal Raman microscope (XperRAM S Series, Nanobase, Korea) with an x50 objective lens and laser power of 3 mW. The acquisitions were carried out with 3x3 $\mu m^2$ unit pixels for a 170 x 80 $\mu m^2$ area. The exposure time for each point was 100 ms.

# IV. RESULTS AND DISCUSSION

## 4.1. Characterization of $(GT)_{15}$-SWNT

SWNT was functionalized by ssDNA with a sequence of $(GT)_{15}$. Flexibility in bond torsion between sugar and phosphate in the $(GT)_{15}$ helped strong interaction between base and SWNT [79]. $(GT)_{15}$ easily bound to the sidewall of the SWNT using mild sonication by strong π-π interaction between the aromatic ring of bases in the $(GT)_{15}$ and the hexagonal ring structure in the side wall of the SWNT **(Fig. 1)**. $(GT)_{15}$-SWNT was well dispersed in an aqueous solution because the negatively charged phosphate group of the ssDNA is hydrophilic and induces electrostatic repulsion among SWNT nanoparticles [79] **(Fig. 2A)**. Intrinsic NIR fluorescence of the $(GT)_{15}$-SWNT presented in 900-1200 nm emission region under a 730 nm excitation, which is a characteristic of the well-dispersed SWNT solution **(Fig. 2B)**. The charge of the $(GT)_{15}$-SWNT was about -57.89 mV **(Fig. 2C),** and $(GT)_{15}$-SWNT shows a good hydrodynamic size distribution under 200 nm **(Fig. 2D)**. Excess ssDNA had to be eliminated by centrifugal filter tube (100 kDa) because free ssDNA was likely to interact with $Au^{3+}$ ions or PDDA-AuNPs. Removal of the excess ssDNA was confirmed through the UV-visible spectrometer; the absorbance peak height of the ssDNA at 260 nm decreased

after washing five times **(Fig. 2E)**. According to the calibration curve of $(GT)_{15}$ molecules **(Fig. 2F)**, filtrated excess $(GT)_{15}$ was approximately 0.8576 mg when 166.1 mg/L of the $(GT)_{15}$-SWNT was synthesized, which indicated that 0.8567 mg of the $(GT)_{15}$ was tightly bound on 1 mg of the SWNT.

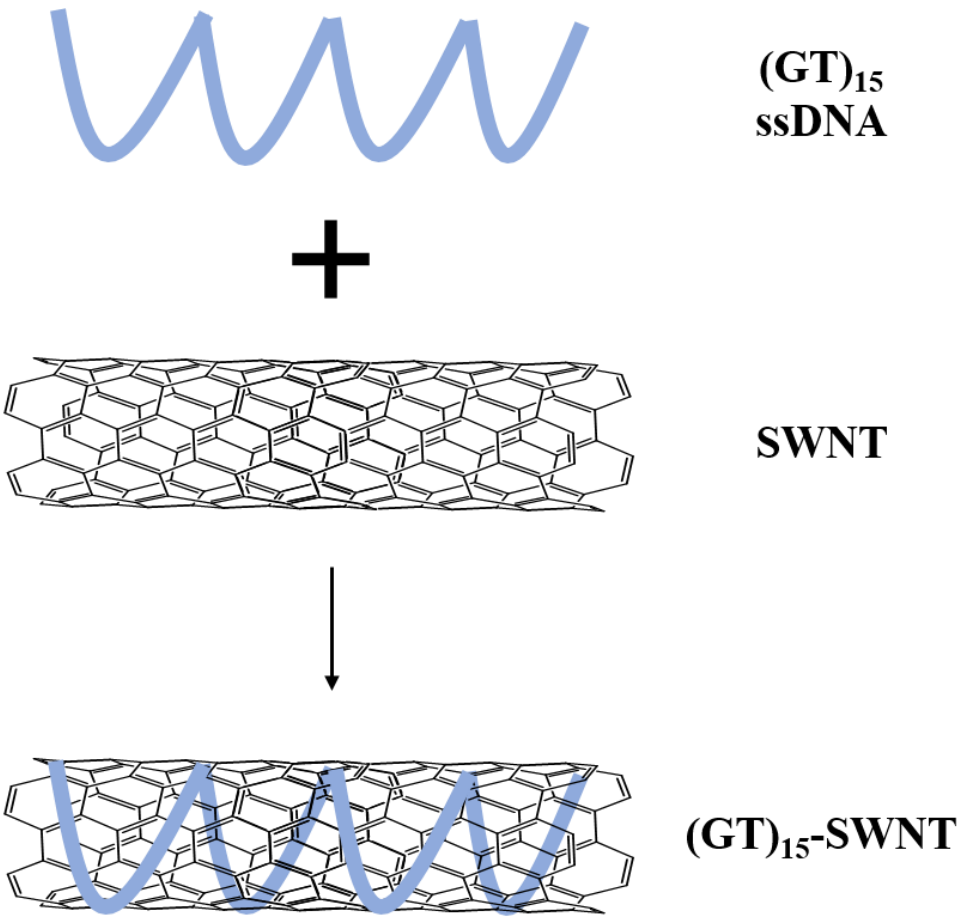


**Figure 1.** Schematic illustration of $(GT)_{15}$-SWNT preparation.

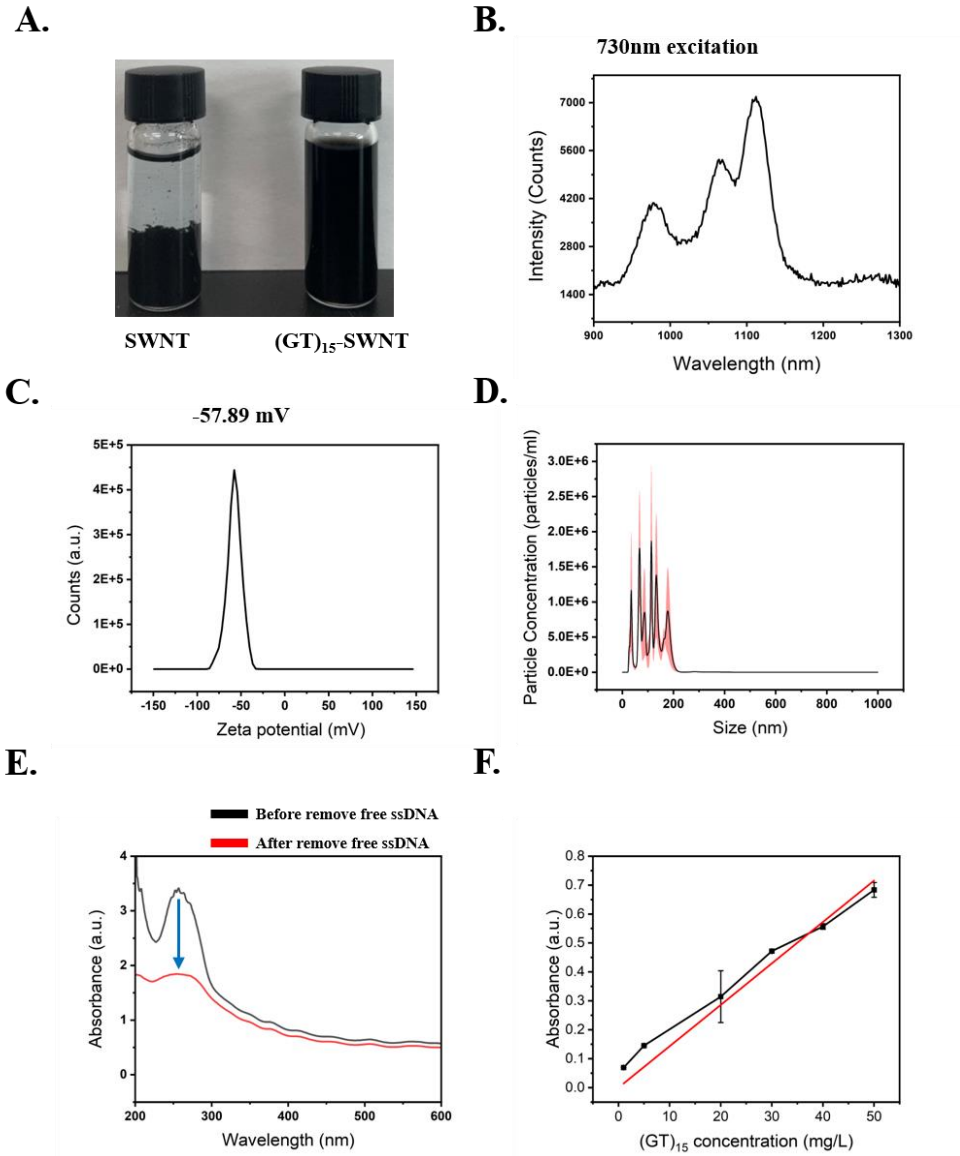


**Figure 2.** Characterization of the $(GT)_{15}$-SWNT. (A) Comparison dispersity between SWNT and $(GT)_{15}$-SWNT in aqueous solution. (B) Fluorescence spectrum of the $(GT)_{15}$-SWNT under 730 nm laser excitation. (C) Charge and (D) size of the $(GT)_{15}$-SWNT. (E) UV-Visible absorbance spectra before and after remove free ssDNA by 100 kDa centrifugal filter devices. (F) Standard absorbance curve of the ssDNA with a sequence of the $(GT)_{15}$

## 4.2. Gold nanoparticle decorated $(GT)_{15}$-SWNT

### 4.2.1. Gold nanoparticle growth on $(GT)_{15}$-SWNT

The $(GT)_{15}$-SWNT was selected as the SERS template for several reasons. First, the phosphate groups are uniformly presented along the side wall of the $(GT)_{15}$-SWNT, which can help the ordered decoration of the AuNPs on the SWNT template. Second, the strong Raman G band of the $(GT)_{15}$-SWNT at 1590 $cm^{-1}$ could be utilized to analyze the location of the nanosensor in living plants [95]. In other words, if oxidized SWNT or graphene oxide (GO) was used as the SERS template, it was challenging to observe the nanosensor's location because of their weak Raman G band. Lastly, according to a previous study, the $(GT)_{15}$-SWNT was biocompatible in living plants, so it was suitable for *in vivo* nanosensors [25]. AuNP was used for SERS substrates to form a strong electromagnetic field. It is also more stable than other noble metals such as silver and copper, and biocompatible with the living organism [96, 97].

AuNPs grew along the sidewall of the $(GT)_{15}$-SWNT via 2 steps, gold seeding and reduction of gold ions **(Fig. 3)**. Negative charge of the phosphate groups in the $(GT)_{15}$ reduced $Au^{3+}$ ions to $Au^{0}$ atoms, so 8.8 nm size gold seeds (Au seeds) were placed on the $(GT)_{15}$-SWNT (**Fig. 4A**). Additional $Au^{3+}$ ions and L-ascorbic acids were added to the solution for increasing diameter of the AuNPs. The $Au^{0}$ atoms, reduced by the L-ascorbic acids,

reacted with the Au seeds on the $(GT)_{15}$-SWNT, increasing AuNPs' diameter. As a result, the UV-visible absorbance spectra of AuNP-SWNT became broader **(Fig. 4B)** upon increasing the concentration of $Au^{3+}$ ions.

AuNPs display an unique optical property called localized surface plasmon resonance, which is the collective oscillation of electrons in the conduction band of AuNP that resonate with a specific wavelength of the incident light, which is dependent on the size and aggregation of the AuNPs [98, 99]. As-prepared AuNPs showed a strong absorbance in 520 nm-580 nm, measured by UV-vis spectroscopy **(Fig 4B)**. Also, the Raman intensity of a model Raman label, 4-bromothiophenol (4-BBT), at 1066 $cm^{-1}$ increased **(Fig. 4C)** accordingly, probably due to the increased size of the AuNPs **(Fig. 4D-F)**. When 0.5 and 1 mM of the Au ions were added, broad peaks were presented in the UV-visible spectra because AuNPs were assembled while maintaining their shape. On the other hand, AuNPs agglomerated to a single mass when 5 mM of the Au ions were added, so a narrow peak was shown in the UV-Visible spectrum **(Fig. 4D-F)**.

Unfortunately, the AuNPs were not successfully assembled on the $(GT)_{15}$-SWNT. Instead, this enhancement is primarily because of the agglomeration of AuNPs; the nanogap size between the AuNPs became narrower in an uncontrollable way, resulting in the formation of stronger electromagnetic fields [100]. Raman intensity of SWNT at 1590 $cm^{-1}$ was supposed to be enhanced by the SERS effect if AuNPs were assembled on the SWNT

template [43, 44, 57]. However, the Raman intensity of the $(GT)_{15}$-SWNT did not be enhanced in the AuNP@SWNT at any gold ion concentration (**Fig. 4C)**. Furthermore, sizes of the AuNPs were varied, and some agglomerates were formed in the solution, not on the $(GT)_{15}$-SWNT in TEM micrographs (**Fig. 4F**). It was probably because $Au^0$ atoms hardly react with gold seeds on the $(GT)_{15}$-SWNT but they self-assembled in solution. In addition, the absence of common stabilizing agents such as cetyltrimethylammonium bromide (CTAB) [101] or polyvinylpyrrolidone (PVP) [102] might cause the aggregation of AuNPs.

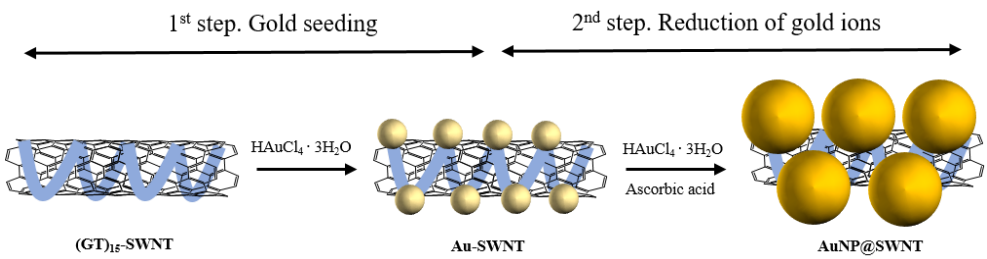


**Figure 1.** Schematic illustration of AuNP growth on the $(GT)_{15}$-SWNT.

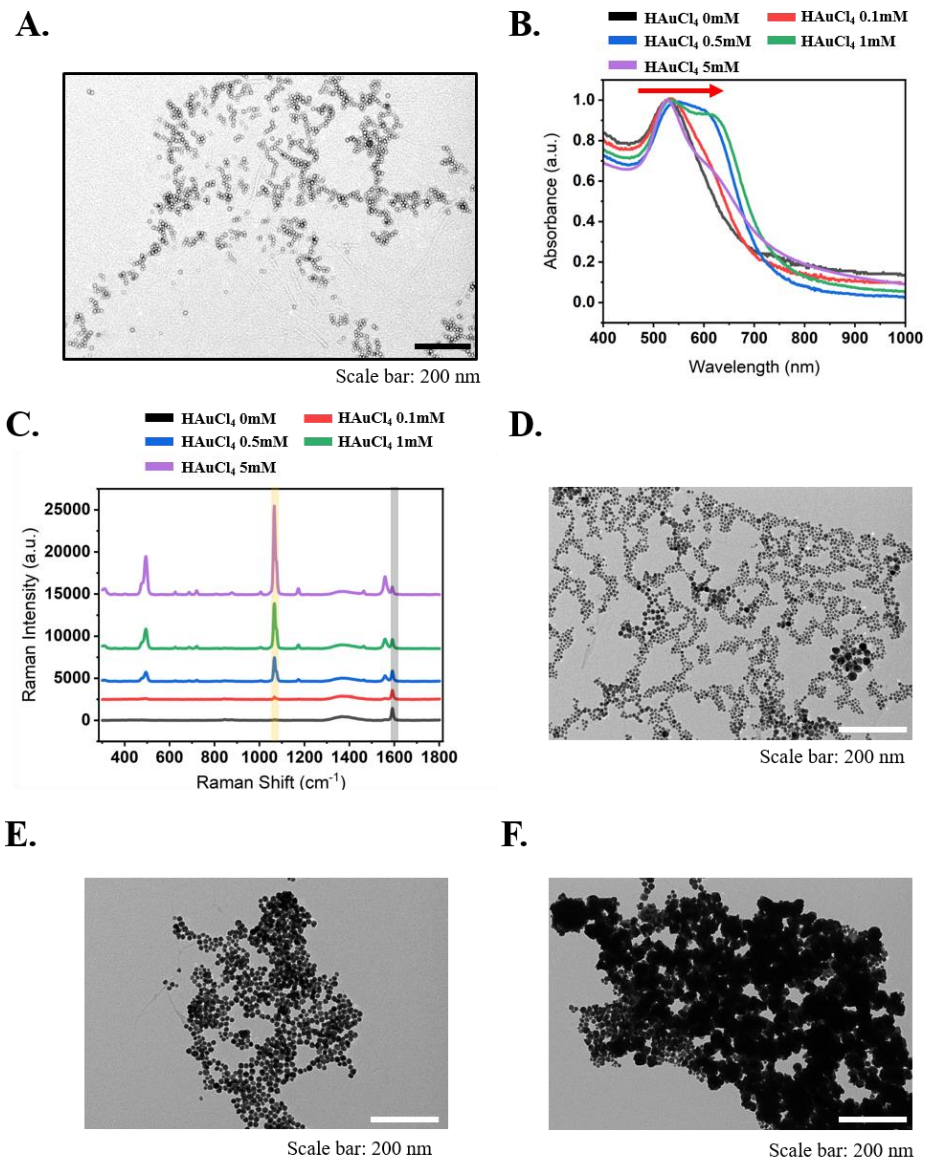


**Figure 2.** Analysis of the AuNP grown on the $(GT)_{15}$-SWNT. (A) TEM images of Au seeds on the $(GT)_{15}$-SWNT. (B) UV-Visible spectra and (C) SERS spectrum of AuNP@SWNT with 100 μM 4-BBT for different $Au^{3+}$ ion concentrations. SERS spectra were acquired with a 660 nm laser at 25mW. (D-F) TEM image of the AuNP@SWNT for different $Au^{3+}$ ion concentration. Scale bar, 200 nm. (D: $HAuCl_4$ 0.5 mM, E: $HAuCl_4$ 1 mM, F: $HAuCl_4$ 5 mM)

### 4.2.2. PDDA capped gold nanoparticle decorated $(GT)_{15}$-SWNT

PDDA is a quaternary ammonium cationic polymer. It acted as both the reducing and stabilizing agents in the AuNP synthesis protocol **(Fig. 5)** [92]. Amine groups of the PDDA reduced the $Au^{3+}$ ions to the $Au^{0}$ atoms and generated a positive charge on the surface of the AuNPs, stabilizing AuNPs by preventing aggregation [103, 104]. The size of the PDDA-AuNPs was measured through TEM images, and it was about 17.52 nm **(Fig. 6A)**. A standard curve was prepared based on the absorbance using commercially available 20 nm gold nanoparticles to estimate the concentration of the PDDA-AuNPs **(Fig. 6B).** Both the standard gold nanoparticles and our PDDA-AuNPs had maximum absorbance at 518~522nm in the UV-visible spectrum. **(Fig. 6C).** PDDA-AuNPs had a strong positive charge (49.59 mV) **(Fig. 6C)** and were monodisperse **(Fig. 6D)** compared to the AuNPs formed by rapid reduction with L-ascorbic acid **(Fig.4D)**.

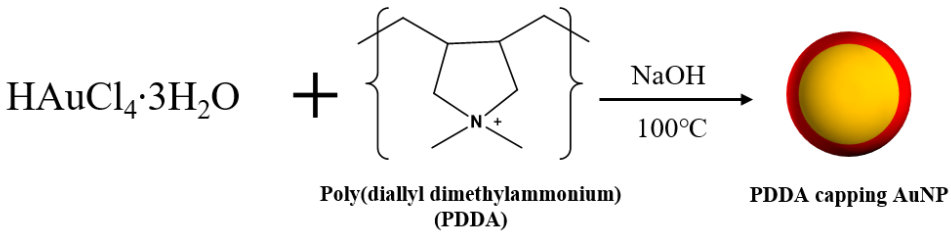


**Figure 3.** Schematic illustration of PDDA-AuNP synthesis protocol. PDDA was used for both reducing and stabilizing agent and NaOH adjusted suitable pH value, which is important in synthesize of the PDDA-AuNP.

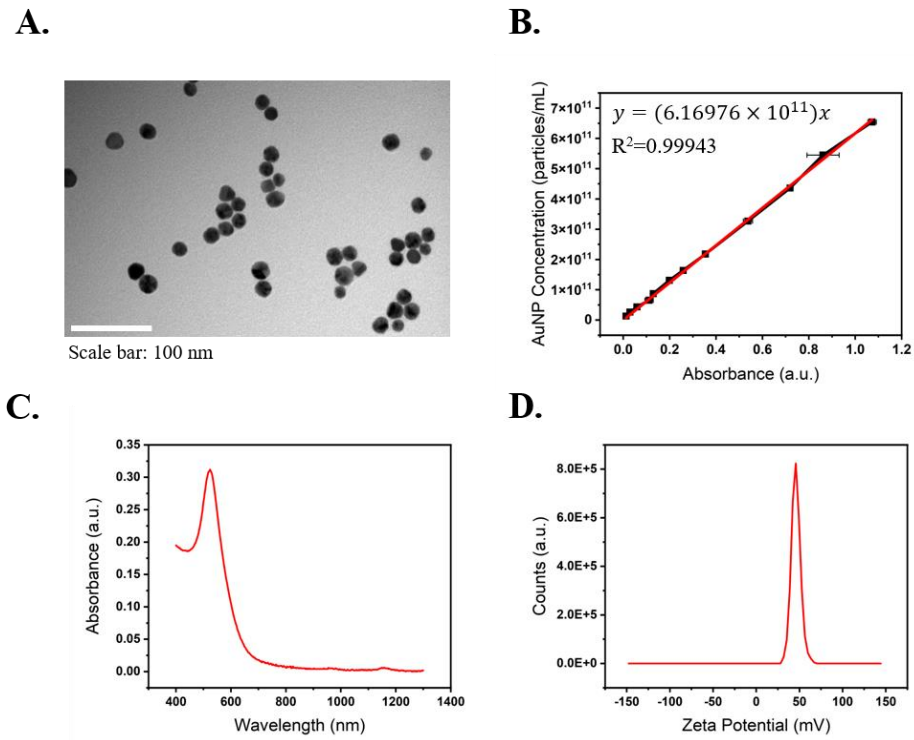


**Figure 4.** Characterization of PDDA-AuNP. (A) TEM image of PDDA-AuNP. Scale bar, 100 nm. (B) Standard absorbance curve of the commercial available 20 nm AuNP. (C) UV-visible spectra and (D) surface charge of the PDDA-AuNP.

PDDA-AuNPs were assembled on the surface of the $(GT)_{15}$-SWNT by electrostatic interaction between the PDDA-AuNPs and the $(GT)_{15}$-SWNT **(Fig. 7)**. Phosphate groups of the $(GT)_{15}$-SWNT provided uniform binding sites for the decoration of the PDDA-AuNPs on the SWNT template. As a result, the UV-visible absorbance spectra of the PDDA-AuNP@SWNT shifted toward red wavelength and became broader compared to that of the PDDA-AuNP **(Fig. 8A)**. As the number of the AuNPs on the SWNT increased, the degree of change in the UV-visible absorbance spectra increased **(Fig. 8A)**. The color of the PDDA-AuNP@SWNT solution also changed red to purple. The average charge of the PDDA-AuNP@SWNT was -35.31 mV; the absolute value of the surface charge is lower than that of the $(GT)_{15}$-SWNT **(Fig. 8B)**. It seemed that the concentration of the AuNPs rarely affected the charge of the PDDA-AuNP@SWNT, but it had an effect on the charge distribution. The charge distribution of the PDDA-AuNP@SWNT with 0.5 x $10^{12}$ particles/mL AuNPs was broader than that of the other samples because AuNPs were sparsely assembled on the $(GT)_{15}$-SWNT **(Fig. 8C)**. SERS band intensity of a model Raman label, 4-FBT, at 1072 $cm^{-1}$ increased when the more PDDA-AuNPs assembled on the $(GT)_{15}$-SWNT **(Fig. 8D)**. This enhancement is because the nanogap size between the AuNPs became narrower as the number of the AuNP increases, resulting in the formation of stronger electromagnetic fields [100]. However, the colloidal stability of the PDDA-AuNP@SWNT with 2.0 x $10^{12}$ particles/mL AuNPs was not stable so it aggregated after a few minutes. Thus, an optimized condition was selected

for PDDA-AuNP@SWNT with 1.5 x $10^{12}$ particles/mL. PDDA-AuNPs were aligned on the sidewall of the $(GT)_{15}$-SWNT as shown in TEM micrographs **(Fig. 8E)**. Also, nanogap between the PDDA-AuNPs was under 2 nm, which was appropriate to create hot spots **(Fig. 8F)**. SWNT Raman peak at 1590 $cm^{-1}$ was amplified due to the hot spots created by the tightly assembled PDDA-AuNPs on the $(GT)_{15}$-SWNT. **(Fig. 9A)**.

The enhancement factor(EF) is an important parameter to evaluate the SERS effect [105]. EF of as-prepared PDDA-AuNP@SWNT was obtained by Eq. 3.

$$\text{(Enhancement factor)} = \left(\frac{I_{SERS}}{I_{NR}}\right) \times \left(\frac{N_{NR}}{N_{SERS}}\right) \quad \textbf{(Eq. 3)}$$

$I_{SERS}$ and $I_{NR}$ are the SERS and normal Raman intensity of 4-FBT, known as a standard Raman label. $I_{SERS}$ and $I_{NR}$ were obtained as 8250 and 15891 (a.u.), respectively **(Fig. 9B).** $N_{NR}$ is the number of 4-FBT in focal volume and $N_{SERS}$ is the number of 4-FBT on the surface of the PDDA-AuNPs. $N_{NR}$ and $N_{SERS}$ were obtained by Eq. 4 and 5.

$$N_{NR} = \frac{N_A \times V_{focal} \times d_{4\text{-FBT}}}{M_{4\text{-FBT}}} \quad \textbf{(Eq. 4)}$$

$$N_{SERS} = \frac{C_{AuNP} \times V_{focal} \times S_{AuNP}}{S_{4\text{-FBT, Au}}} \quad \textbf{(Eq. 5)}$$

In Eq. 3, $N_A$ is Avogadro number, $V_{focal}$ is the focal volume of the laser, $d_{4\text{-FBT}}$ is the density of the 4-FBT (1.203 g/mL), and $M_{4\text{-FBT}}$ is the molecular

weight of the 4-FBT (128.17 g/mol). $C_{AuNP}$ is the concentration of the AuNP ($1.5 \times 10^{12}$ particles/mL), and $S_{AuNP}$ is the surface area of the AuNP ($289\pi$ $nm^2$). $S_{4\text{-}FBT,\ Au}$ is the area occupied by one 4-FBT molecule on the AuNP surface (0.383 $nm^2$/molecule)[106] in Eq. 4. As a result, the EF of AuNP@SWNT was $4.07 \times 10^6$ much higher than the EF of single AuNPs ($10^3$~$10^4$) [29]. SERS spectrum of 4-FBT was obtained after 5 weeks to assess the stability of the PDDA-AuNP@SWNT in aqueous conditions at ambient temperature **(Fig. 9C)**. SERS intensity at 1072 $cm^{-1}$ was not significantly changed over 5 weeks.

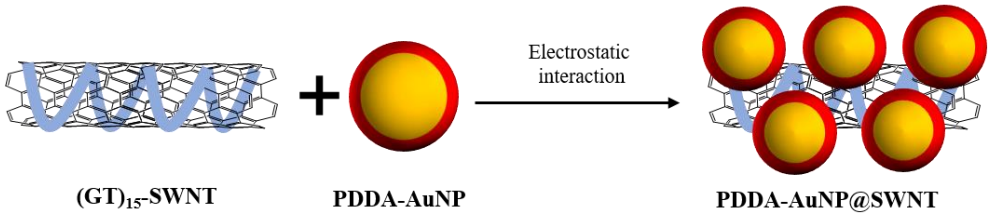


**Figure 5.** Schematic illustration of preparing PDDA-AuNP assembly on the $(GT)_{15}$-SWNT. The PDDA-AuNP and $(GT)_{15}$-SWNT interacted through the electrostatic interaction.

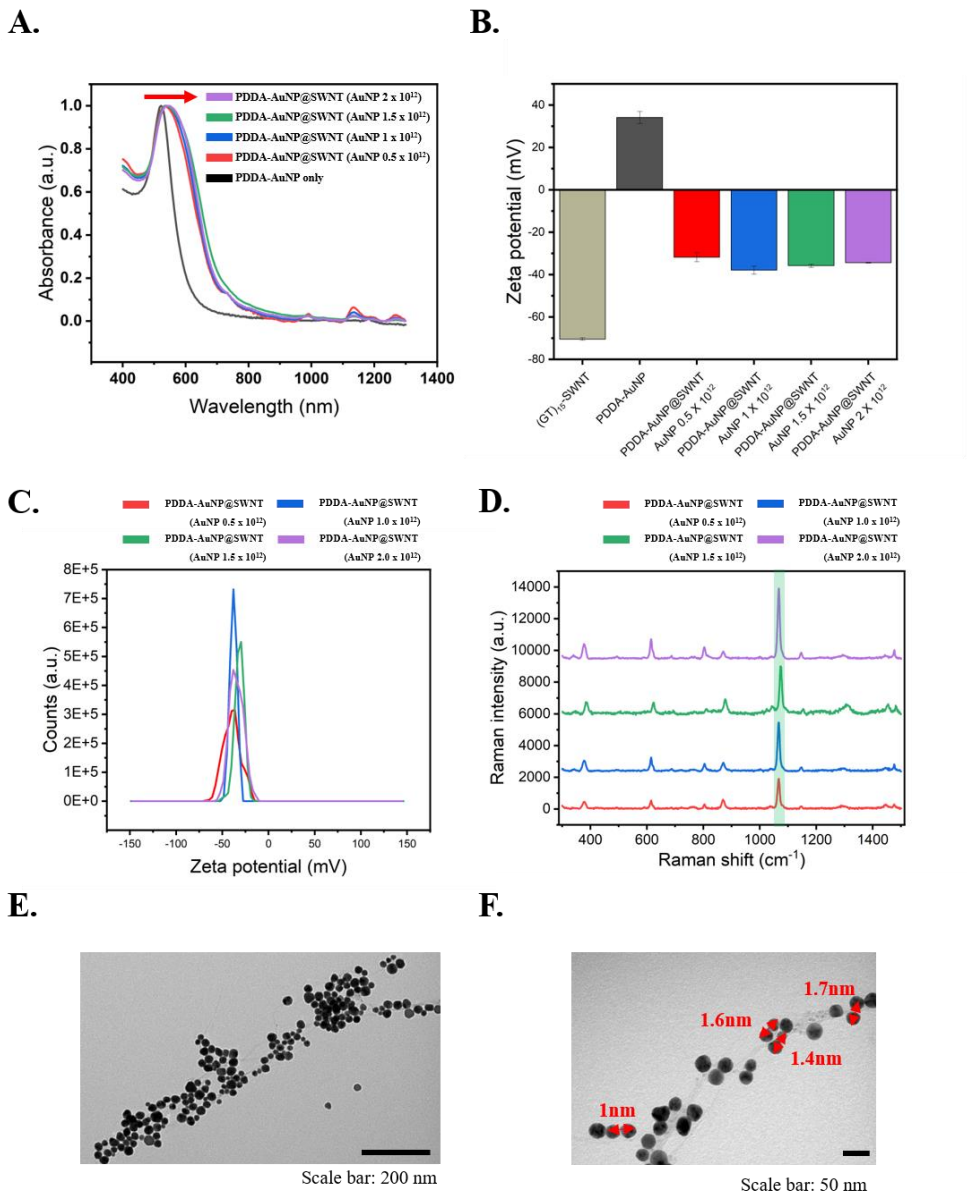


**Figure 6.** Analysis of PDDA-AuNP@SWNT. (A) UV-Visible spectra of the PDDA-AuNP@SWNT for different AuNP concentration. (B) Average surface charge of $(GT)_{15}$-SWNT, PDDA-AuNP and PDDA-AuNP@SWNT for different AuNP concentration. (C) Zeta potential distribution of the PDDA-AuNP@SWNT for different AuNP concentration (D) SERS spectrum of the PDDA-AuNP@SWNT with 100 μM 4-FBT for different AuNP concentration. SERS spectra were obtained with a 600 nm laser at 25 mW. (E, F) TEM image of PDDA-AuNP@SWNT with 1.5 x $10^{12}$ particles/mL for 100k and 315k magnification. Scale bar, 200 and 50 nm, respectively.

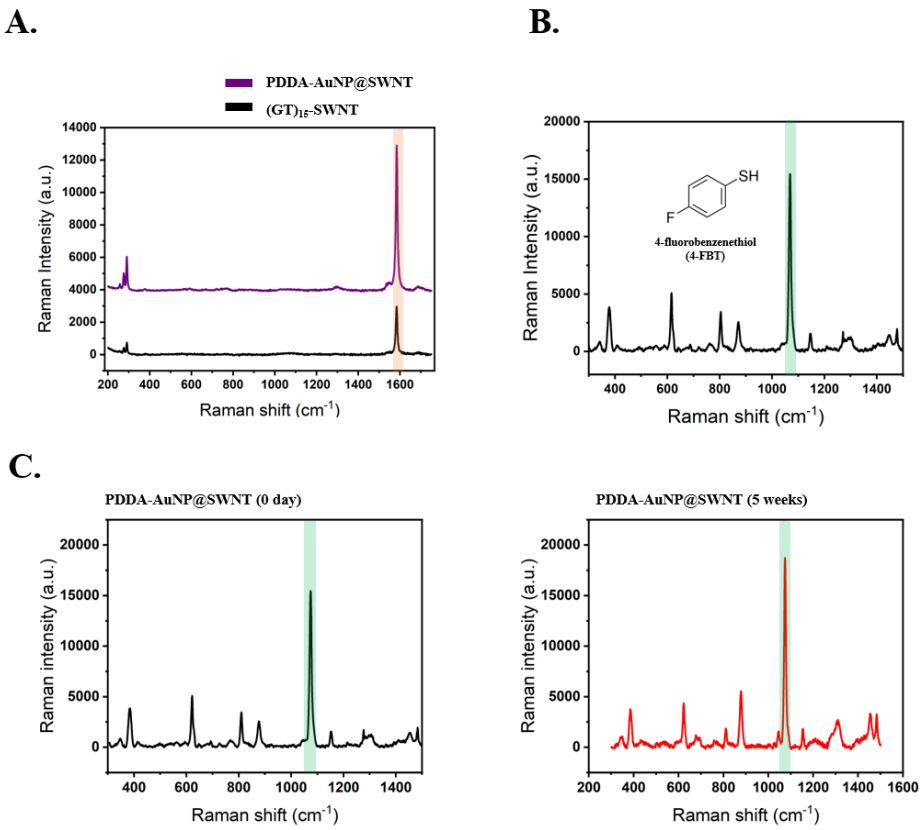


**Figure 7.** Raman and SERS spectra using PDDA-AuNP@SWNT. (A) Raman spectra of $(GT)_{15}$-SWNT and PDDA-AuNP@SWNT. (B) SERS spectrum of 1mM 4-FBT obtained with PDDA-AuNP@SWNT. (C) SERS spectra of 1mM 4-FBT using PDDA-AuNP@SWNT after 0 day and 5 weeks. All spectra were obtained with a 660 nm laser at 25 mW.

## 4.3. Multiplex detection of endogenous plant signaling molecules *in vitro*

Multiplex detection of endogenous plant signaling molecules is necessary for a more accurate understanding of plant health. eATP, thiamine, and nasturlexin B were selected as target signaling molecules released to activate the plant defense system under wound stresses. Locating the signaling molecules near the hot spots is essential to detect a trace amount of analytes in the living plants. Therefore, the AuNPs surface was functionalized with PDDA for attracting eATP to the hot spot through electrostatic interaction and multiple hydrogen bonds [107, 108]. The hydrogen bond between PDDA and ATP is different from the classical hydrogen bonding; the $CH_2$ backbone of the PDDA forms a hydrogen bond with the adenine group of the ATP because carbon can serve as a hydrogen donor or acceptor [109, 110]. Likewise, thiamine and nasturlexin B could be attracted to the hot spot since their sulfide groups can strongly interact with the Au surface [111].

*In vitro* SERS spectra of ATP, thiamine, and 2-TAT were obtained using PDDA-AuNP@SWNT, and each distinct SERS band was presented **(Fig. 10A)**. The commercially available chemical 2-TAT was used as a substitute for nasturlexin B because it possesses the same thiazoline moiety **(Fig. 10B)**.

ATP SERS spectrum showed a characteristic band at 730 $cm^{-1}$ corresponding to the adenosine ring, thiamine had distinct bands at 751 and

929 $cm^{-1}$ corresponding to pyrimidine and thiazole rings [112], and 2-TAT exhibited three strong bands at 650, 1020 and 1340 $cm^{-1}$ [113]. Three kinds of plant stress-related biomolecules were mixed, added to the PDDA-AuNP@SWNT suspension, and then the SERS spectrum was obtained to validate multiplex detection of the nanosensor **(Fig. 10A)**. All fingerprint SERS bands of each molecule were shown in SERS spectrum of the mixture. The PDDA-AuNP@SWNT could detect multiple signaling molecules simultaneously, allowing us to quickly identify them by the Raman fingerprint pattern with narrow width.

**A.**

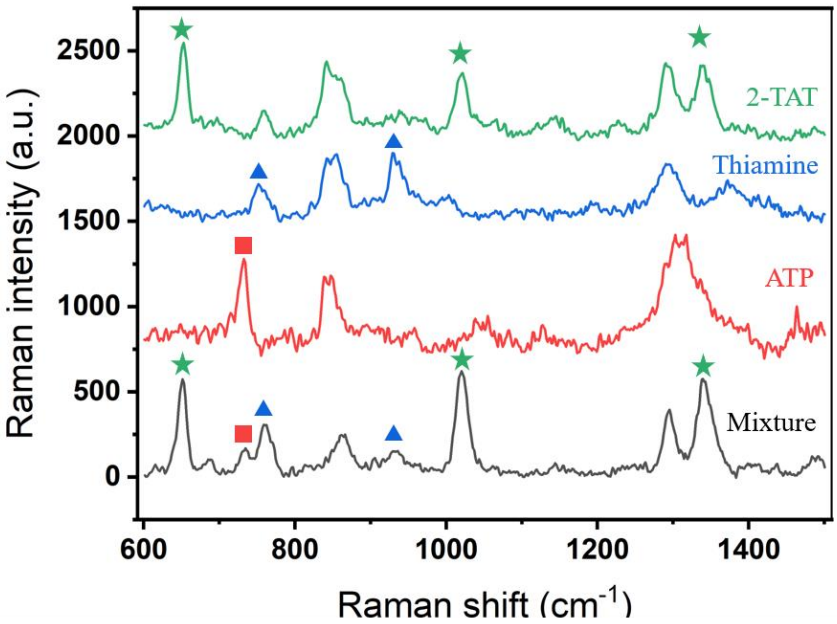


**B.**

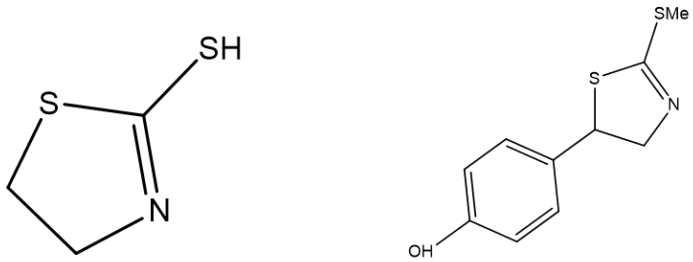


**2-thiazoline-2-thiol (2-TAT)**

**Nasturlexin B**

**Figure 8.** Multiplex detection of stress-dependent molecules *in vitro*. (A) SERS spectra of various plant signaling molecules, 2-TAT (green), TA (Blue), ATP (Red) and mixture (black). Concentration of each molecules was 100 μM. SERS spectra were obtained with a 785 nm laser at 13 mW. (B) Structure of 2-TAT and nastrulexin B.

## 4.4. Biocompatibility of PDDA-AuNP@SWNT in plants

Biocompatibility is one of the critical properties that *in vivo* nanosensors must have [114]. Biocompatibility of the PDDA-AuNP@SWNT in the living plants was evaluated by measuring the concentration of the chlorophyll [25] and the propidium iodide (PI) assay [115]. The chlorophyll concentration was measured for 2 weeks in nanosensor-embedded watercress leave and buffer-infiltrated ones (control). Chlorophyll contents of the nanosensor-embedded watercress leaf decreased over time but were not significantly different from that of the control **(Fig. 11A)**. PI is a fluorescent dye used to stain the cells and DNA. It was widely used to evaluate cell viability because PI interacts with bases of DNA and is impermeable to the cell membrane of healthy cells [116, 117]. When the plants are under stable conditions, PI stays outside plant cells since it cannot penetrate the cell wall [118]. However, if the nanosensor damages the plant cell, PI penetrates the inside area of the plant cell and forms a complex with cellular DNA. It was found that the nanosensor induced no cell death or severe cellular stress **(Fig. 11B)**. Nanosensor was infiltrated into the watercress through the pore on the epidermis area. The size of the stomata is about 3.8±0.6 μm, and there were 17.2±2.5 stomata per 1 $mm^2$ of the watercress epidermis area, large enough for the nanosensor infiltration **(Fig. 11C)**.

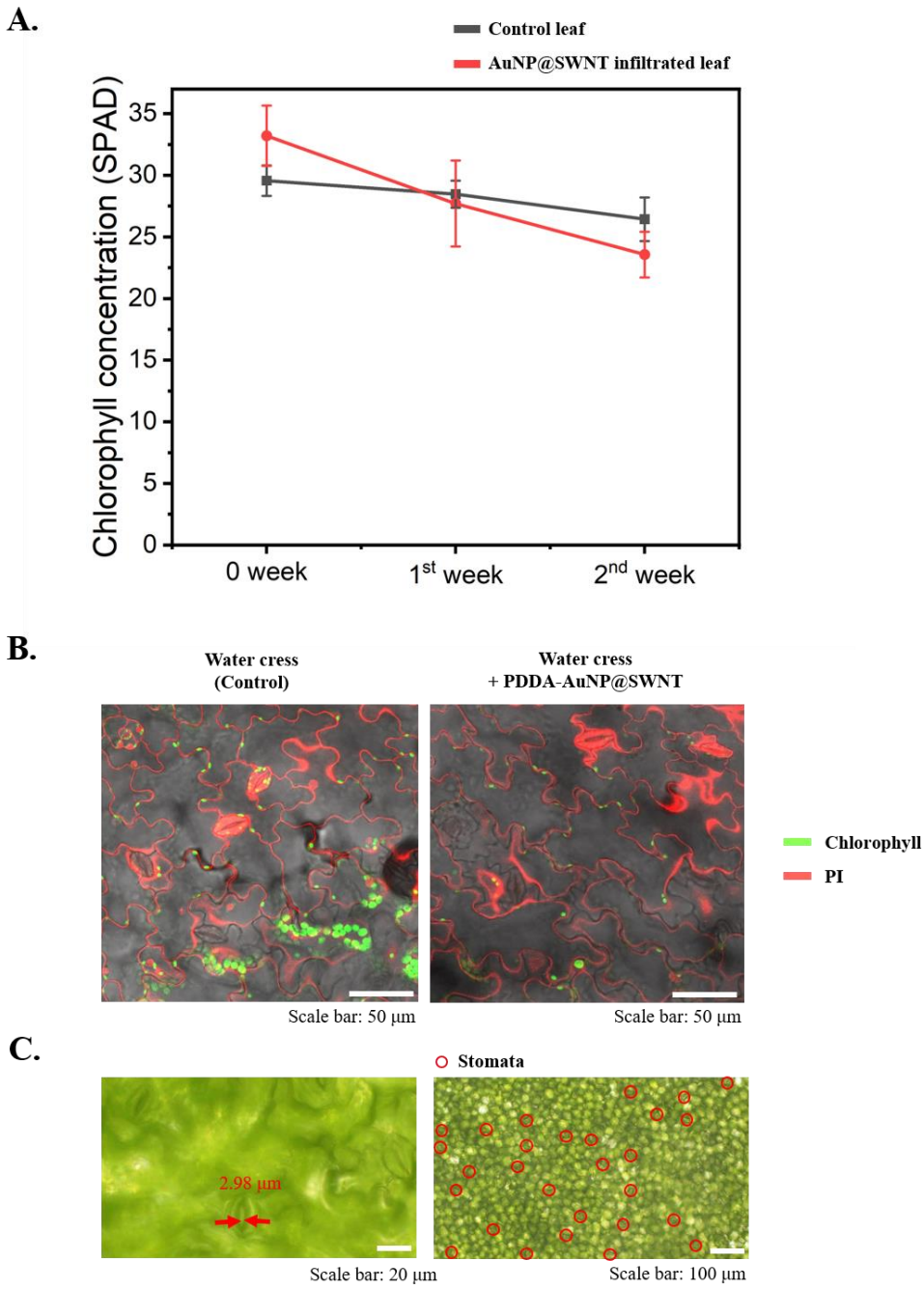


**Figure 9.** Biocompatibility of AuNP@SWNT in watercress. (A) Measurement of chlorophyll concentration for 2 weeks. (B) CLSM images of PI stained nanosensor infiltrated watercress and control watercress. Scale bar, 50 μm. (C) Microscope images of the epidermis of the watercress (Left: x40, Right: x10). Scale bar, 20 and 100 μm.

## 4.5. Monitoring of wound signal in living plants using nanosensor

Attack by herbivores and insects causes wounds on the leaf, severely threatening plants. In addition, wound places are prone to infection by various viruses and pathogens, so plants release several signaling molecules to activate the defense system. Therefore, it is crucial to detect these wound signaling molecules before visible symptoms to minimize damage from the wound stress.

PDDA-AuNP@SWNT was infiltrated into the watercress leaf to detect the plant signaling molecules **(Fig. 12A)**. Location of the PDDA-AuNP@SWNT in the living plants was easily identified by SERS mapping due to the strong G band of the $(GT)_{15}$-SWNT at 1590 $cm^{-1}$. SERS mapping was carried out under 785 nm laser excitation to circumvent autofluorescence from the chlorophyll in plant leaf tissue and acquired 700 μm away from the wound to avoid the intense fluorescence from the damaged plant cells. SERS mapping confirmed that the nanosensors were deposited along the plant cell walls in the epidermis area **(Fig. 12B)**. It was similar to the previous studies, where the nanoparticles such as silica nanoparticles and the SWNT were located in the intercellular junctions [95, 119]. PDDA-AuNP@SWNT could detect nasturlexin B, signaling molecules in cruciferous plants, from the watercress leaf upon wound stress. Nasturlexin B is a signaling molecule

known to be biosynthesized explicitly in the watercress leaves to resist various stresses, especially wounding [20]. Although stress signals can be generated from different parts of plants, SERS mapping was carried out on leaves rather than other parts of the plants, such as roots, as leaves are easier to collect the SERS signals from living plants. In addition, stress signaling molecules are transported to the leaf through apoplastic routes so that stress signaling molecules can be detected in the leaf. The nanosensor detected nasturlexin B in spots A and B after the wound **(Fig. 13A and B)**. SERS bands of the thiazoline moiety in the nasturlexin B at 650, 1020, and 1340 $cm^{-1}$ were shown in the SERS spectrum, which was identical to the SERS bands in 2-TAT *in vitro* SERS spectrum. However, signals did not appear in all areas where the nanosensors were present. This variance indicates that some plant cells produce signaling molecules while others do not respond to wound stress simultaneously.

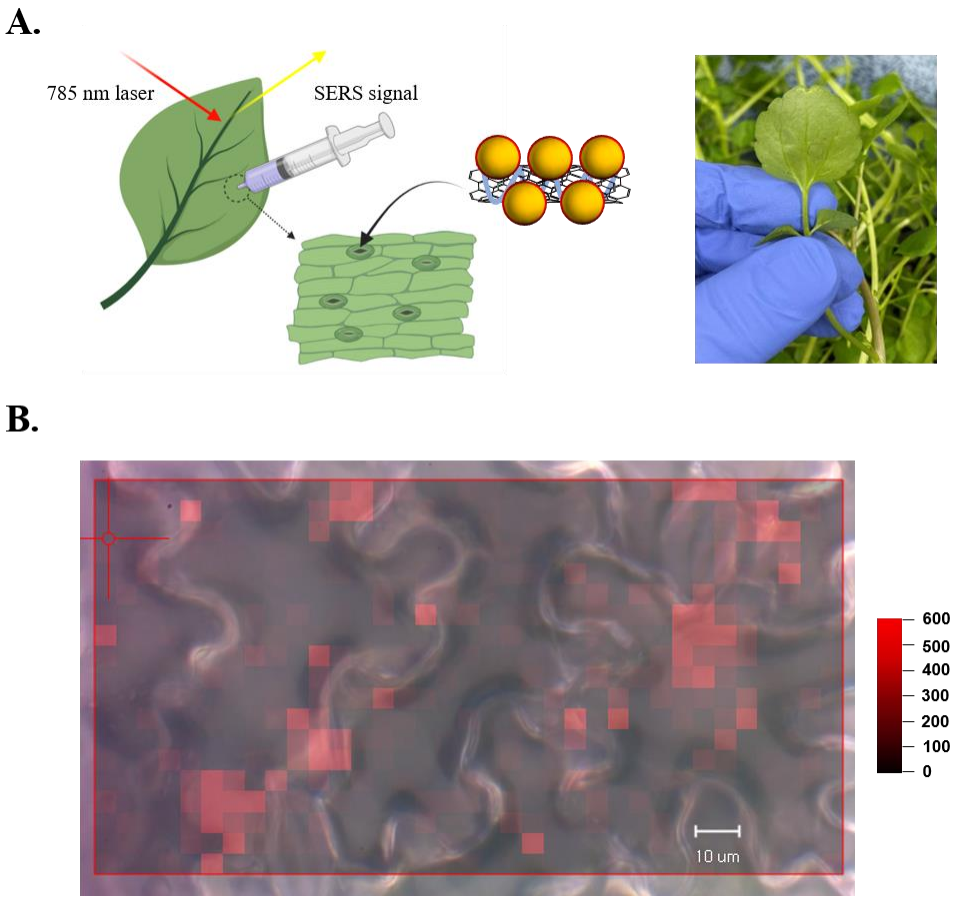


**Figure 10.** Introduction of PDDA-AuNP@SWNT in living plants. (A) Schematic illustration of nanosensor infiltration to watercress and image of nanosensor embedded watercress leaf. (B) PDDA-AuNP@SWNT location in epidermis area of the watercress. Raman mapping image at 1590 $cm^{-1}$ was acquired under 785 nm laser at 3 mW. Scale bar, 10 μm.

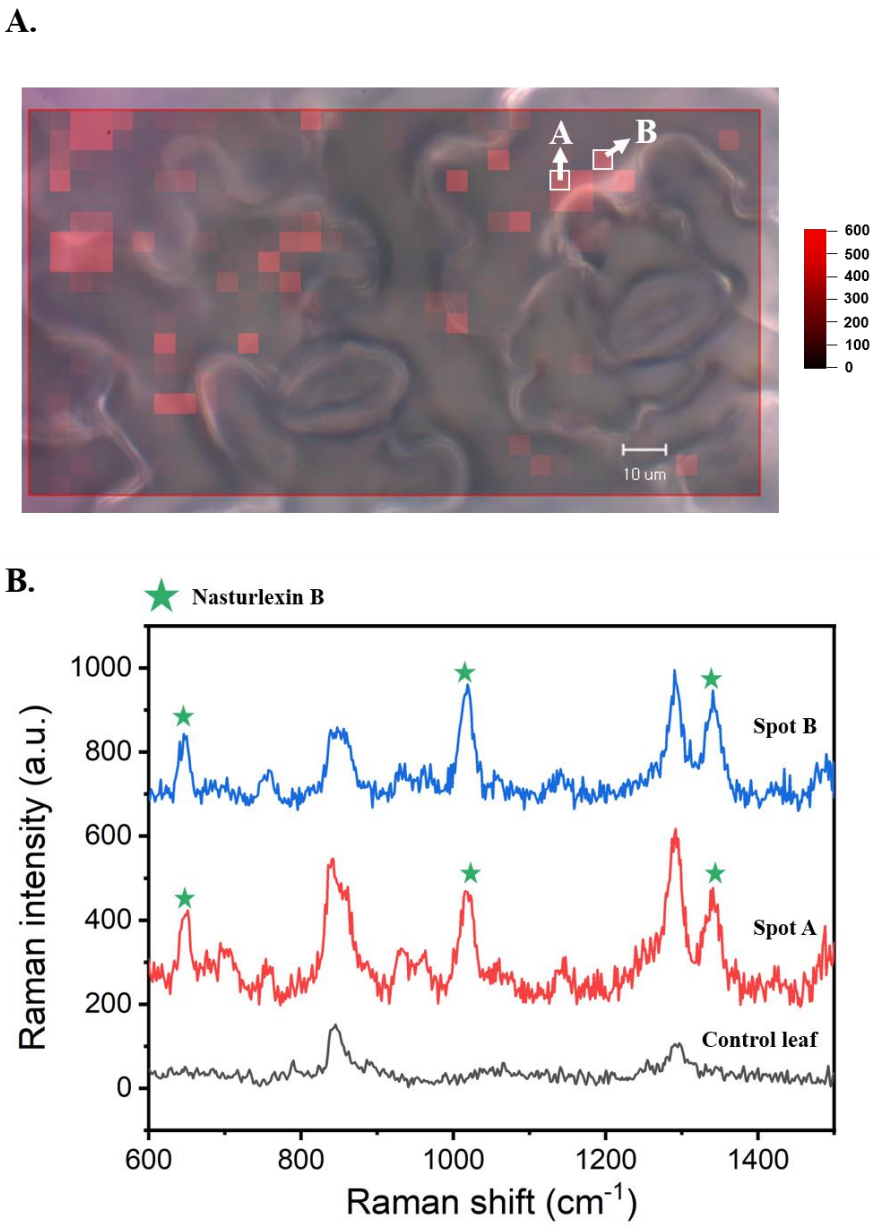


**Figure 11.** Detection of the plants signaling molecule using PDDA-AuNP@SWNT. (A) Overlay of the SERS mapping and bright field images of the epidermis area. SERS mapping image at 1590 $cm^{-1}$ was acquired under 785 nm laser at 3 mW. Scale bar, 10 μm. (B) SERS spectra in different spot of the living plants after wound stress. SERS spectra were obtained with a 785 nm laser at 3 mW. Exposure time was 100 ms.

# V. CONCLUSION

In this study, the SWNT-based SERS nanosensor was fabricated for detecting plants' stress-induced signaling molecules in living plants. SWNT was functionalized with ssDNA $(GT)_{15}$ for increasing dispersity in an aqueous solution and provided ordered binding sites for PDDA-AuNPs assembly. PDDA-AuNP@SWNT was active in the NIR region, capable of circumventing the strong chlorophyll fluorescence. TEM micrographs and a change in the UV-visible spectrum confirmed PDDA-AuNP assembly on the SWNT. The enhancement factor was $4.07 \times 10^6$, which was higher than the enhancement factor of the single AuNPs. The nanosensor detected three signaling molecules in plants: ATP, thiamine, and nasturlexin B. The biocompatibility of the nanosensor in living plants was demonstrated by chlorophyll content measurement and PI assay. The location of the nanosensor in the plants was analyzed by the strong Raman band of the SWNT at 1590 $cm^{-1}$. One of the plant signaling molecules, nasturlexin B, was successfully detected using the nanosensor after the wound in the living plants. However, some hurdles must be overcome to apply this nanosensor for monitoring plant health. First, detecting more various signaling molecules is required in future work to monitor other stresses like cold and pathogens.

Furthermore, introducing this nanosensor in important agricultural crops

such as wheat, barley, and maize is necessary to manage the crop supply. Lastly, obtaining a SERS spectrum with a high signal-to-noise ratio using portable Raman spectrometers is essential to applying the nanosensor in the field. Therefore, this SERS nanosensor platform will greatly help the agriculture field if these problems are solved in the future.

# REFERENCES


1. Tilman, D., Balzer, C., Hill, J., et al., *Global food demand and the sustainable intensification of agriculture.* Proceedings of the National Academy of Sciences, 2011. **108**(50): p. 20260-20264.

2. World Health Organization., *The state of food security and nutrition in the world 2020: transforming food systems for affordable healthy diets*. Vol. 2020. 2020: Food & Agriculture Org.

3. Lee, G., Q. Wei, and Y. Zhu, *Emerging wearable sensors for plant health monitoring.* Advanced Functional Materials, 2021. **31**(52): p. 2106475.

4. Gull, A., A.A. Lone, and N.U.I. Wani, *Biotic and abiotic stresses in plants.* Abiotic and Biotic Stress in Plants, 2019: p. 1-19.

5. Dal Bello, G., Monaco, C., Rollan, MC., et al., *Biocontrol of postharvest grey mould on tomato by yeasts.* Journal of Phytopathology, 2008. **156**(5): p. 257-263.

6. Xu, X.-M. and A. Berrie. *Use of a disease forecasting system to manage strawberry grey mould*. in *VII International Strawberry Symposium 1049*. 2012: p. 613-619

7. Pimentel, D. and M. Burgess, *Environmental and economic costs of the application of pesticides primarily in the United States*, in *Integrated Pest Management*. 2014, Springer. p. 47-71.

8. Shakir, S.K., Irfan, S., Akhtar, B., et al., *Pesticide-induced oxidative stress and antioxidant responses in tomato (Solanum lycopersicum) seedlings.* Ecotoxicology, 2018. **27**(7): p. 919-935.

9. Hatamleh, A.A., Danish, M., Al-Dosary, M. A., et al., *Physiological and oxidative stress responses of Solanum lycopersicum (L.)(tomato) when exposed to different chemical pesticides.* RSC Advances, 2022. **12**(12): p. 7237-7252.

10. Durrant, W.E. and X. Dong, *Systemic acquired resistance.* Annual Review of Phytopathology, 2004. **42**(1): p. 185-209.

11. Kushalappa, A.C., K.N. Yogendra, and S. Karre, *Plant innate immune response: qualitative and quantitative resistance.* Critical Reviews in Plant Sciences, 2016. **35**(1): p. 38-55.

12. Pieterse, C.M., Leon-Reyes, A., Van der Ent, S., et al., *Networking by small-molecule hormones in plant immunity.* Nature Chemical Biology, 2009. **5**(5): p. 308-316.

13. Jeandet, P., *Phytoalexins: current progress and future prospects.* Molecules, 2015. **20**(2): p. 2770-2774.

14. Jeandet, P., Hébrard, C., Deville, M. A., et al., *Deciphering the role of phytoalexins in plant-microorganism interactions and human health.* Molecules, 2014. **19**(11): p. 18033-18056.

15. Chivasa, S., Murphy, A. M., Hamilton, J. M., et al., *Extracellular ATP is a regulator of pathogen defence in plants.* The Plant Journal, 2009. **60**(3): p. 436-448.

16. Gaffney, T., Friedrich, L., Vernooij, B., et al., *Requirement of salicylic acid for the induction of systemic acquired resistance.* Science, 1993. **261**(5122): p. 754-756.

17. Fitzpatrick, T.B. and L.M. Chapman, *The importance of thiamine (vitamin B1) in plant health: From crop yield to biofortification.* Journal of Biological Chemistry, 2020. **295**(34): p. 12002-12013.

18. Yusof, Z.N.B., *Thiamine and its role in protection against stress in plants (enhancement in thiamine content for nutritional quality improvement)*, in *Nutritional Quality Improvement in Plants*. 2019, Springer. p. 177-186.

19. Pedras, M.S.C. and Q.H. To, *Non-indolyl cruciferous phytoalexins: Nasturlexins and tridentatols, a striking convergent evolution of defenses in terrestrial plants and marine animals?* Phytochemistry, 2015. **113**: p. 57-63.

20. Pedras, M.S.C. and Q.H. To, *Interrogation of biosynthetic pathways of the cruciferous phytoalexins nasturlexins with isotopically labelled compounds.* Organic & Biomolecular Chemistry, 2018. **16**(19): p. 3625-3638.

21. War, A.R., et al., Paulraj, M. G., Ahmad, T., *Mechanisms of plant*

*defense against insect herbivores.* Plant Signaling & Behavior, 2012. **7**(10): p. 1306-1320.

22. Mittler, R., Zandalinas, S. I., Fichman, Y., et al., *Reactive oxygen species signalling in plant stress responses.* Nature Reviews Molecular Cell Biology, 2022. **23**(10): p. 663-679.

23. Hu, J. and Y. Xianyu, *When nano meets plants: A review on the interplay between nanoparticles and plants.* Nano Today, 2021. **38**: p. 101143.

24. Yan, Y., Ni, M., Wang, F., et al., *Metal–Organic Framework-Based Biosensor for Detecting Hydrogen Peroxide in Plants through Color-to-Thermal Signal Conversion.* ACS Nano, 2022. **16**(9):p. 15175-15187.

25. Lew, T.T.S., et al., Koman, V. B., Silmore, K. S., et al., *Real-time detection of wound-induced $H_2O_2$ signalling waves in plants with optical nanosensors.* Nature Plants, 2020. **6**(4): p. 404-415.

26. Shauloff, N., N.L. Teradal, and R. Jelinek, *Porous graphene oxide–metal ion composite for selective sensing of organophosphate gases.* ACS Sensors, 2020. **5**(6): p. 1573-1581.

27. Logan, N., Haughey, S. A., Liu, L., et al., *Handheld SERS coupled with QuEChERs for the sensitive analysis of multiple pesticides in basmati rice.* npj Science of Food, 2022. **6**(1): p. 1-11.

28. Lew, T.T.S., Koman, V. B., Gordiichuk, P., et al., *The emergence of plant nanobionics and living plants as technology.* Advanced Materials Technologies, 2020. **5**(3): p. 1900657.

29. Ding, S.-Y., Yi, J., Li, J., et al., *Nanostructure-based plasmon-enhanced Raman spectroscopy for surface analysis of materials.* Nature Reviews Materials, 2016. **1**(6): p. 1-16.

30. Anker, J.N., Hall, W. P., Lyandres, O., et al., *Biosensing with plasmonic nanosensors.* Nature Materials, 2008. **7**(6): p. 442-453.

31. Zong, C., Xu, M., Xu, L., et al., *Surface-enhanced Raman spectroscopy for bioanalysis: reliability and challenges.* Chemical Reviews, 2018. **118**(10): p. 4946-4980.

32. Petryayeva, E. and U.J. Krull, *Localized surface plasmon resonance: Nanostructures, bioassays and biosensing—A review.* Analytica Chimica Acta, 2011. **706**(1): p. 8-24.

33. McMahon, J.M., Li, S., Ausman, L. K., et al., *Modeling the effect of small gaps in surface-enhanced Raman spectroscopy.* The Journal of Physical Chemistry C, 2012. **116**(2): p. 1627-1637.

34. Ding, S.-Y., You, E. M., Tian, Z. Q., et al., *Electromagnetic theories of surface-enhanced Raman spectroscopy.* Chemical Society Reviews, 2017. **46**(13): p. 4042-4076.

35. Langer, J., Jimenez de Aberasturi, D., Aizpurua, J., et al., *Present and future of surface-enhanced Raman scattering.* ACS Nano, 2019. **14**(1): p. 28-117.

36. De Gelder, J., De Gussem, K., Vandenabeele, P., et al., *Reference database of Raman spectra of biological molecules.* Journal of Raman Spectroscopy: An International Journal for Original Work in all Aspects of Raman Spectroscopy, Including Higher Order Processes, and also Brillouin and Rayleigh Scattering, 2007. **38**(9): p. 1133-1147.

37. Ambartsumyan, O., Gribanyov, D., Kukushkin, V., et al., *SERS-based biosensors for virus determination with oligonucleotides as recognition elements.* International Journal of Molecular Sciences, 2020. **21**(9): p. 3373.

38. Moore, T.J., Moody, A. S., Payne, T. D., et al., *In vitro and in vivo SERS biosensing for disease diagnosis.* Biosensors, 2018. **8**(2): p. 46.

39. Jaworska, A., Fornasaro, S., Sergo, V., et al., *Potential of surface enhanced Raman spectroscopy (SERS) in therapeutic drug monitoring (TDM). A critical review.* Biosensors, 2016. **6**(3): p. 47.

40. Markina, N.E., Ustinov, S. N., Zakharevich, A. M., et al., *Copper nanoparticles for SERS-based determination of some cephalosporin antibiotics in spiked human urine.* Analytica Chimica Acta, 2020. **1138**: p. 9-17.

41. Liu, C., Xu, T., Cheng, G., et al., *Target-triggered regioselective assembly of nanoprobes for Raman imaging of dual cancer biomarkers in living cells.* Sensors and Actuators B: Chemical, 2021. **330**: p. 129319.

42. Wang, W., Zhao, F., Li, M., et al., *A SERS Optophysiological Probe for the Real-Time Mapping and Simultaneous Determination of the Carbonate Concentration and pH Value in a Live Mouse Brain.* Angewandte Chemie International Edition, 2019. **58**(16): p. 5256-5260.

43. Wang, X., Wang, C., Cheng, L., et al., *Noble metal coated single-walled carbon nanotubes for applications in surface enhanced Raman scattering imaging and photothermal therapy.* Journal of the American Chemical Society, 2012. **134**(17): p. 7414-7422.

44. Song, J., Wang, F., Yang, X., et al., *Gold nanoparticle coated carbon nanotube ring with enhanced raman scattering and photothermal conversion property for theranostic applications.* Journal of the American Chemical Society, 2016. **138**(22): p. 7005-7015.

45. Li, J., Yan, H., Tan, X., et al., *Cauliflower-inspired 3D SERS substrate for multiple mycotoxins detection.* Analytical chemistry, 2019. **91**(6): p. 3885-3892.

46. Bennett, J. and M. Klich, *Clinical microbiology reviews.* Mycotoxins, 2003. **16**(1): p. 497-516.

47. Yang, D., Afroosheh, S., Lee, J. O., et al., *Glucose sensing using surface-enhanced Raman-mode constraining.* Analytical Chemistry, 2018. **90**(24): p. 14269-14278.

48. Andreou, C., Hoonejani, M. R., Barmi, M. R., et al., *Rapid detection of drugs of abuse in saliva using surface enhanced Raman spectroscopy and microfluidics.* ACS Nano, 2013. **7**(8): p. 7157-7164.

49. Zaytseva, O. and G. Neumann, *Carbon nanomaterials: production, impact on plant development, agricultural and environmental applications.* Chemical and Biological Technologies in Agriculture, 2016. **3**(1): p. 1-26.

50. Power, A.C., Gorey, B., Chandra, S., et al., *Carbon nanomaterials and their application to electrochemical sensors: a review.* Nanotechnology Reviews, 2018. **7**(1): p. 19-41.

51. Hong, G., Diao, S., Antaris, A. L., et al., *Carbon nanomaterials for biological imaging and nanomedicinal therapy.* Chemical Reviews, 2015. **115**(19): p. 10816-10906.

52. Zhu, Z., Yang, R., You, M., et al., *Single-walled carbon nanotube as an effective quencher.* Analytical and Bioanalytical Chemistry, 2010. **396**(1): p. 73-83.

53. Kasry, A., Ardakani, A. A., Tulevski, G. S., et al., *Highly efficient fluorescence quenching with graphene.* The Journal of Physical Chemistry C, 2012. **116**(4): p. 2858-2862.

54. Liang, X., Li, N., Zhang, R., et al., *Carbon-based SERS biosensor: From substrate design to sensing and bioapplication.* NPG Asia Materials, 2021. **13**(1): p. 1-36.

55. Bhunia, S.K., Zeiri, L., Manna, J., et al., *Carbon-dot/silver-nanoparticle flexible SERS-active films.* ACS Applied Materials & Interfaces, 2016. **8**(38): p. 25637-25643.

56. Caires, A., Vaz, R. P., Fantini, C., et al., *Highly sensitive and simple SERS substrate based on photochemically generated carbon nanotubes–gold nanorods hybrids.* Journal of Colloid and Interface Science, 2015. **455**: p. 78-82.

57. Ondera, T.J. and A.T. Hamme II, *A gold nanopopcorn attached single-walled carbon nanotube hybrid for rapid detection and killing of bacteria.* Journal of Materials Chemistry B, 2014. **2**(43): p. 7534-7543.

58. Jabłońska, A.,Jaworska, A., Kasztelan, M., et al., *Graphene and graphene oxide applications for SERS sensing and imaging.* Current Medicinal Chemistry, 2019. **26**(38): p. 6878-6895.

59. Jain, A., Homayoun, A., Bannister, C. W., et al., *Single-walled carbon nanotubes as near-infrared optical biosensors for life sciences and biomedicine.* Biotechnology Journal, 2015. **10**(3): p. 447-459.

60. Bati, A.S., Yu, L., Batmunkh, M., et al., *Recent Advances in Applications of Sorted Single-Walled Carbon Nanotubes.* Advanced Functional Materials, 2019. **29**(30): p. 1902273.

61. Zhang, D., Xia, C., Li, S., et al., *Detection of Off-Resonance Single-Walled Carbon Nanotubes by Enormous Surface-Enhanced Raman Scattering.* Advanced Optical Materials, 2021. **9**(20): p. 2100559.

62. Ursu, E.-L., Doroftei, F., Peptanariu, D., et al., *DNA-assisted decoration of single-walled carbon nanotubes with gold nanoparticles for applications in surface-enhanced Raman scattering imaging of cells.* Journal of Nanoparticle Research, 2017. **19**(5): p. 1-9.

63. Hendler-Neumark, A. and G. Bisker, *Fluorescent single-walled carbon nanotubes for protein detection.* Sensors, 2019. **19**(24): p. 5403.

64. Li, R., Wu, R. A., Zhao., et al., *P-glycoprotein antibody functionalized carbon nanotube overcomes the multidrug resistance of human leukemia cells.* ACS Nano, 2010. **4**(3): p. 1399-1408.

65. Cho, S.-Y., Jin, X., Gong, X., et al., *Antibody-free rapid detection of SARS-CoV-2 proteins using corona phase molecular recognition to accelerate development time.* Analytical Chemistry, 2021. **93**(44): p. 14685-14693.

66. Giraldo, J.P., Landry, M. P., Kwak, S. Y., et al., *A ratiometric sensor using single chirality near-infrared fluorescent carbon nanotubes: Application to in vivo monitoring.* Small, 2015. **11**(32): p. 3973-3984.

67. Kwak, S.-Y., Lew, T. T. S., Sweeney, C. J., et al., *Chloroplast-selective gene delivery and expression in planta using chitosan-complexed single-walled carbon nanotube carriers.* Nature Nanotechnology, 2019. **14**(5): p. 447-455.

68. Lew, T.T.S., Park, M., Wang, Y., et al., *Nanocarriers for transgene expression in pollen as a plant biotechnology tool.* ACS Materials Letters, 2020. **2**(9): p. 1057-1066.

69. Jackson, C.T., Wang, J. W., González-Grandío, E., et al., *Polymer-conjugated carbon nanotubes for biomolecule loading.* ACS Nano, 2021. **16**(2): p. 1802-1812.

70. Mallakpour, S. and S. Soltanian, *Surface functionalization of carbon nanotubes: Fabrication and applications.* RSC Advances, 2016. **6**(111): p. 109916-109935.

71. Peng, X. and S.S. Wong, *Functional covalent chemistry of carbon nanotube surfaces.* Advanced Materials, 2009. **21**(6): p. 625-642.

72. Zhao, Y.-L. and J.F. Stoddart, *Noncovalent functionalization of single-walled carbon nanotubes.* Accounts of Chemical Research, 2009. **42**(8): p. 1161-1171.

73. Liu, Z., Tabakman, S., Welsher, K., et al., *Carbon nanotubes in biology and medicine: in vitro and in vivo detection, imaging and drug delivery.* Nano Research, 2009. **2**(2): p. 85-120.

74. Liu, Z., Sun, X., Nakayama-Ratchford, N., et al., *Supramolecular chemistry on water-soluble carbon nanotubes for drug loading and delivery.* ACS Nano, 2007. **1**(1): p. 50-56.

75. Palacin, T., Khanh, H. L., Jousselme, B., et al., *Efficient functionalization of carbon nanotubes with porphyrin dendrons via click chemistry.* Journal of the American Chemical Society, 2009. **131**(42): p. 15394-15402.

76. Sánchez-Tirado, E., González-Cortés, A., Yáñez-Sedeño, P., et al., *Carbon nanotubes functionalized by click chemistry as scaffolds for the preparation of electrochemical immunosensors. Application to the determination of TGF-beta 1 cytokine.* Analyst, 2016. **141**(20): p. 5730-5737.

77. Datsyuk, V., Kalyva, M., Papagelis, K., et al., *Chemical oxidation of multiwalled carbon nanotubes.* Carbon, 2008. **46**(6): p. 833-840.

78. Setaro, A., Adeli, M., Glaeske, M., et al., *Preserving π-conjugation in covalently functionalized carbon nanotubes for optoelectronic applications.* Nature Communications, 2017. **8**(1): p. 1-7.

79. Zheng, M., Jagota, A., Semke, E. D., et al., *DNA-assisted dispersion and separation of carbon nanotubes.* Nature Materials, 2003. **2**(5): p. 338-342.

80. Simmons, T.J., Bult, J., Hashim, D. P., et al., *Noncovalent functionalization as an alternative to oxidative acid treatment of single wall carbon nanotubes with applications for polymer composites.* ACS Nano, 2009. **3**(4): p. 865-870.

81. Compton, O.C. and S.T. Nguyen, *Graphene oxide, highly reduced graphene oxide, and graphene: versatile building blocks for carbon-based materials.* Small, 2010. **6**(6): p. 711-723.

82. Papageorgiou, D.G., I.A. Kinloch, and R.J. Young, *Mechanical properties of graphene and graphene-based nanocomposites.* Progress in Materials Science, 2017. **90**: p. 75-127.

83. Chen, D., H. Feng, and J. Li, *Graphene oxide: preparation, functionalization, and electrochemical applications.* Chemical Reviews, 2012. **112**(11): p. 6027-6053.

84. Wang, Z., Wu, S., Ciacchi, L. C., et al., *Graphene-based nanoplatforms for surface-enhanced Raman scattering sensing.* Analyst, 2018. **143**(21): p. 5074-5089.

85. Lai, H., Xu, F., Zhang, Y., et al., *Recent progress on graphene-based substrates for surface-enhanced Raman scattering applications.* Journal of Materials Chemistry B, 2018. **6**(24): p. 4008-4028.

86. Iliut, M., Leordean, C., Canpean, V., et al., *A new green, ascorbic acid-assisted method for versatile synthesis of Au–graphene hybrids as efficient surface-enhanced Raman scattering platforms.* Journal of Materials Chemistry C, 2013. **1**(26): p. 4094-4104.

87. Hu, C., Rong, J., Cui, J., et al., *Fabrication of a graphene oxide–gold nanorod hybrid material by electrostatic self-assembly for surface-enhanced Raman scattering.* Carbon, 2013. **51**: p. 255-264.

88. Hsu, K.-C. and D.-H. Chen, *Microwave-assisted green synthesis of Ag/reduced graphene oxide nanocomposite as a surface-enhanced Raman scattering substrate with high uniformity.* Nanoscale Research Letters, 2014. **9**(1): p. 1-9.

89. Koornneef, A. and C.M. Pieterse, *Cross talk in defense signaling.* Plant Physiology, 2008. **146**(3): p. 839-844.

90. Yin, H., Cao, Y., Marelli, B., et al., *Soil sensors and plant wearables for smart and precision agriculture.* Advanced Materials, 2021. **33**(20): p. 2007764.

91. Zhang, Y., Li, L., Zhang, H., et al., *Ultrasensitive detection of plant hormone abscisic acid-based surface-enhanced Raman spectroscopy aptamer sensor.* Analytical and Bioanalytical Chemistry, 2022. **414**(8): p. 2757-2766.

92. Malassis, L., Dreyfus, R., Murphy, R. J., et al., *One-step green synthesis of gold and silver nanoparticles with ascorbic acid and their versatile surface post-functionalization.* RSC Advances, 2016. **6**(39): p. 33092-33100.

93. Yu, Y., Chen, Z., He, S., et al., *Direct electron transfer of glucose oxidase and biosensing for glucose based on PDDA-capped gold nanoparticle modified graphene/multi-walled carbon nanotubes electrode.* Biosensors and Bioelectronics, 2014. **52**: p. 147-152.

94. Fuller, M. and I. Köper, *Polyelectrolyte-coated gold nanoparticles: the effect of salt and polyelectrolyte concentration on colloidal stability.* Polymers, 2018. **10**(12): p. 1336.

95. Lew, T.T.S., Wong, M. H., Kwak, S. Y., et al., *Rational design principles for the transport and subcellular distribution of nanomaterials into plant protoplasts.* Small, 2018. **14**(44): p. 1802086.

96. Bansal, S.A., Kumar, V., Karimi, J., et al., *Role of gold nanoparticles in advanced biomedical applications.* Nanoscale Advances, 2020. **2**(9): p. 3764-3787.

97. Nejati, K., Dadashpour, M., Gharibi, T., et al., *Biomedical applications of functionalized gold nanoparticles: a review.* Journal of Cluster Science, 2022. **33**(1): p. 1-16.

98. Zuber, A., Purdey, M., Schartner, E., et al., *Detection of gold nanoparticles with different sizes using absorption and fluorescence based method.* Sensors and Actuators B: Chemical, 2016. **227**: p. 117-127.

99. Huang, X. and M.A. El-Sayed, *Gold nanoparticles: Optical properties and implementations in cancer diagnosis and photothermal therapy.* Journal of Advanced Research, 2010. **1**(1): p. 13-28.

100. Ramirez-Perez, J.C., Reis, T. A., Olivera, C. L., et al., *Impact of silver nanoparticles size on SERS for detection and identification of filamentous fungi.* Spectrochimica Acta Part A: Molecular and Biomolecular Spectroscopy, 2022. **272**: p. 120980.

101. Khan, Z., Singh, T., Hussain, J. I., et al., *Au (III)–CTAB reduction by ascorbic acid: Preparation and characterization of gold nanoparticles.* Colloids and Surfaces B: Biointerfaces, 2013. **104**: p. 11-17.

102. Hussain, M.H., Abu Bakar, N. F., Mustapa, A. N., et al., *Synthesis of various size gold nanoparticles by chemical reduction method with different solvent polarity.* Nanoscale Research Letters, 2020. **15**(1): p. 1-10.

103. Newman, J. and G. Blanchard, *Formation of gold nanoparticles using amine reducing agents.* Langmuir, 2006. **22**(13): p. 5882-5887.

104. Yuan, L. and Y. He, *Effect of surface charge of PDDA-protected gold nanoparticles on the specificity and efficiency of DNA polymerase chain reaction.* Analyst, 2013. **138**(2): p. 539-545.

105. Le Ru, E.C., Blackie, E., Meyer, M., et al., *Surface enhanced Raman scattering enhancement factors: a comprehensive study.* The Journal of Physical Chemistry C, 2007. **111**(37): p. 13794-13803.

106. Jiang, P., Deng, K., Fichou, D., et al., *STM imaging ortho-and para-fluorothiophenol self-assembled monolayers on Au (111).* Langmuir, 2009. **25**(9): p. 5012-5017.

107. Zhang, K., Yao, S., Li, G., et al., *One-step sonoelectrochemical fabrication of gold nanoparticle/carbon nanosheet hybrids for efficient surface-enhanced Raman scattering.* Nanoscale, 2015. **7**(6): p. 2659-2666.

108. Lv, W., Liu, C., Ma, Y., et al., *Multi-hydrogen bond assisted SERS*

*detection of adenine based on multifunctional graphene oxide/poly (diallyldimethyl ammonium chloride)/Ag nanocomposites.* Talanta, 2019. **204**: p. 372-378.

109. Parajuli, R. and E. Arunan, *XH⋯ C hydrogen bonds in n-alkane-HX (X= F, OH) complexes are stronger than CH⋯ X hydrogen bonds.* Journal of Chemical Sciences, 2015. **127**(6): p. 1035-1045.

110. Dutta, J., Sahu, A. K., Bhadauria, A. S., et al., *Carbon-Centered Hydrogen Bonds in Proteins.* Journal of Chemical Information and Modeling, 2022. **62**(8): p. 1998-2008.

111. Kokkin, D.L., Zhang, R., Steimle, T. C., et al., *Au–S bonding revealed from the characterization of diatomic gold sulfide, AuS.* The Journal of Physical Chemistry A, 2015. **119**(48): p. 11659-11667.

112. Leopold, N., Cîntă-Pînzaru, S., Baia, M., et al., *Raman and surface-enhanced Raman study of thiamine at different pH values.* Vibrational Spectroscopy, 2005. **39**(2): p. 169-176.

113. Chen, T., Kuo, C. S., Chou, Y. C., et al., *Surface-enhanced Raman scattering of adenosine triphosphate molecules.* Langmuir, 1989. **5**(4): p. 887-891.

114. Soto, R.J., Hall, J. R., Brown, M. D., et al., *In vivo chemical sensors: role of biocompatibility on performance and utility.* Analytical Chemistry, 2017. **89**(1): p. 276-299.

115. Kus-Liśkiewicz, M., P. Fickers, and I. Ben Tahar, *Biocompatibility and cytotoxicity of gold nanoparticles: recent advances in methodologies and regulations.* International Journal of Molecular Sciences, 2021. **22**(20): p. 10952.

116. Crowley, L.C., Scott, A. P., Marfell, B. J., et al., *Measuring cell death by propidium iodide uptake and flow cytometry.* Cold Spring Harbor Protocols, 2016. **2016**(7): p. pdb. prot087163.

117. Crowley, L.C., G. Chojnowski, and N.J. Waterhouse, *Measuring the DNA content of cells in apoptosis and at different cell-cycle stages by propidium iodide staining and flow cytometry.* Cold Spring Harbor Protocols, 2016. **2016**(10): p. pdb. prot087247.

118. Dengler, W.A., Schulte, J., Berger, D. P., et al., *Development of a propidium iodide fluorescence assay for proliferation and cytotoxicity assays.* Anti-Cancer Drugs, 1995. **6**(4): p. 522-532.

119. Kwak, S.-Y., Giraldo, J. P., Wong, M. H., et al., *A nanobionic light-emitting plant.* Nano Letters, 2017. **17**(12): p. 7951-7961.

# 국문초록

작물 생산성 증진을 위해서는 가시적인 증상이 나타나기 전에 식물의 스트레스를 진단하는 것이 필요하다. 본 연구에서는 비생물적 스트레스인 상처에 의해 생성되는 식물 신호 분자를 감지하기 위한 단일벽 탄소나노튜브 (SWNT) 기반의 표면증강산란 (SERS) 나노 센서를 제작했다. SWNT를 $(GT)_{15}$ 서열을 가진 단일 가닥 DNA로 기능화 한 (GT)15-SWNT를 금 나노입자를 질서있게 집합시키기 위한 템플릿으로 사용하였다. $(GT)_{15}$-SWNT 표면에서의 L-아스코르브산에 의한 금 나노입자 합성은 통제불가능한 금 나노입자응집을 형성했기 때문에 AuNP를 밀도 있게 위치시키는 데 효과적인 방법이 아니었다. 반면에, PDDA 고분자로 기능화되어 양전하를 띄는 금 나노입자는 정전기적 상호작용을 통해 $(GT)_{15}$-SWNT의 측벽을 따라 조밀하게 위치할 수 있었고, 많은 수의 핫스팟을 성공적으로 생성하였으며 $4.07 \times 10^6$의 enhancement factor 값을 가졌다. SERS 나노센서를 사용하여 nasturlexin B, TA, ATP와 같은 내인성 식물 신호 물질의 SERS 스펙트럼을 얻었으며, 혼합물에서도 각 분석물이 가지는 고유의 SERS 피크가 SERS 스펙트럼에 나타남을 통해 다중검출이 가능함을 확인했다. 식물체 내 SERS 나노센서의 생체적합성은 엽록소의 농도와 PI 분석을 통해 확인했고, SWNT의 강한 라만 신호를 이용해 나노센서가

식물체 내로 잘 도입되었음을 증명했다. 나노센서가 도입된 식물 잎에 상처를 낸 후, 785 nm 레이저를 사용해 얻은 SERS 스펙트럼에서 nasturlexin B 신호를 실시간 검출할 수 있었는데, 이는 물냉이 식물과 같은 십자화과 식물의 주요 스트레스 신호 물질 중 하나이다. 본 연구를 통해 개발된 SERS 나노센서를 이용하면 식물의 스트레스를 지속적으로 모니터링함으로써 농작물 생산성 향상에 기여할 수 있을 것으로 기대된다.